Simulation of Schottky Diode-Based Silicon Carbide Radiation Detectors

Kjetil Moe Gulli

Thesis submitted for the degree of
Master in Materials, Nanophysics and Quantum Technology
60 credits

Department of Physics
Faculty of Mathematics and Natural Sciences

UNIVERSITY OF OSLO

Spring 2022

© 2022 Kjetil Moe Gulli

Simulation of Schottky Diode-Based Silicon Carbide Radiation Detectors

http://www.duo.uio.no/

Printed: Reprosentralen, University of Oslo

Abstract

Physical characterisation and subsequent simulations of Schottky diodes on n-type 4H-SiC were performed. The simulations were then expanded to strip detectors in order to propose a suitable design for a microstrip radiation detector. To do this, a set of 4H-SiC Schottky diodes were characterised through I-V, C-V and DLTS measurements. The experimental results were used to implement numerical models in Silvaco Atlas simulations of the measured diodes. By simulating radiation as a track of released charge carriers, transient simulations were performed to simulate the effect of impacting radiation. Lastly, different strip detector designs were simulated.

Among the characterised diodes, the highest quality diode had an ideality factor of $\eta = 1.03$ and an estimated reverse saturation current $I_0 = (1.6 \pm 0.1) \cdot 10^{-25}$ A. Its simulated counterpart had an ideality factor of $\eta = 1.01$, a reverse saturation current $I_0 = 3.6 \cdot 10^{-27}$ A, and avalanche breakdown at about 1600 V. The doping concentration of the top, epitaxial, layer was found to be between 0.9 and $1.4 \cdot 10^{15}$ cm^{-3} from capacitance measurements, with indications of a doping depth distribution that increased as a function of depth into the epitaxial layer. DLTS identified traps at energies of $E_t = 0.69 \pm 0.01$ eV and $E_t = 0.18 \pm 0.02$ eV below the conduction band, attributed to carbon vacancies ($Z_{1/2}$) and substitutional Ti atoms, respectively. Their respective concentrations were $(2.19 \pm 0.13) \cdot 10^{13}$ cm^{-3} and $N_t = (3.2 \pm 0.3) \cdot 10^{12}$ cm^{-3}.

Simulations with varying concentrations of $Z_{1/2}$ showed little or no impact on detector performance for concentrations up to 10^{15} - 10^{16} cm^{-3}. Capacitance and radiation simulations both showed full depletion of the 10 µm thick epitaxial film at slightly above 100 V, and it was demonstrated that only charges released in this layer induced any detectable current. Simulations of microstrip designs with 10, 20, and 30 µm wide gaps between the electrodes reveal a clear demand for larger voltages when the gaps is wider, and suggest the 20 µm design as preferable for fabrication and further studies.

Acknowledgements

I would like to thank my supervisors Eduard Monakhov, Angela Kok, and Marco Povoli for all your help and feedback. Thank you to Robert Michael Karsthof for helping me with all the physical measurements. Although I do not think I have had the pleasure of meeting you, thank you Ilia Kolevatov for fabricating the Schottky diodes the experimental part is based upon, and thanks to Augustinas Galeckas for giving me custody over said diodes. I should also give thanks to all other employees working with or for the University of Oslo for making this a nice place to undergo an education.

Special thanks to Hilde for your continued love and support, and to Markus for all your input that I try my utmost to disagree with. Finally, I must thank my family for keeping up with me rarely visiting during my studies here in Oslo.

This thesis was written and carried out within the framework of project Novel Silicon Carbide Dosimeter in Radiation Therapy and Radiation Protection (NoSiCaR), funded by the Research Council of Norway, project number 274742.

The Research Council of Norway is acknowledged for the support to the Norwegian Micro- and Nano-Fabrication Facility, NorFab, project number 295864.

Contents

Abstract **i**

Acknowledgements **iii**

Contents **v**

1 Introduction **1**

2 Theory **5**

2.1 Semiconductor Physics 5

2.1.1 Fermi-Dirac Statistics 5

2.1.2 Energy Bands 6

2.1.3 Charge Carriers 7

2.1.4 Doping 10

2.1.5 Carrier Mobility 14

2.2 Diodes 15

2.2.1 P-N Junctions 16

2.2.2 Schottky Diodes 17

2.2.3 Diode-Based Detectors 19

3 Experimental **21**

3.1 I-V 21

3.2 C-V 22

3.3 DLTS 23

3.4 Experimental Details 27

4 Simulations **29**

4.1 Single Diode Simulations 29

4.2 Transient Simulation 31

4.3 Strip Detector Simulations 32

4.4 Physical Models 33

4.4.1 Mobility 34

4.4.2 Carrier Recombination 36

4.4.3 Band Gap Narrowing . . . 36
4.4.4 Contacts . . . 37
4.4.5 Single Event Upset . . . 37

5 Results and Discussion **39**
5.1 Measurements . . . 39
5.1.1 I-V . . . 39
5.1.2 C-V . . . 40
5.1.3 DLTS . . . 42
5.2 Simulation . . . 47
5.2.1 I-V . . . 47
5.2.2 C-V . . . 49
5.2.3 Transient Simulations . . . 50
5.2.4 Strip Detector Model . . . 54

6 Summary **57**
6.1 Conclusion . . . 57
6.2 Future Work . . . 59

A Silvaco Scripts **65**
A.1 I-V and C-V Simulations . . . 65
A.1.1 I-V . . . 65
A.1.2 C-V . . . 65
A.1.3 Script (I-V and C-V) . . . 65
A.2 Transient Simulations . . . 68
A.2.1 CCE vs Voltage . . . 68
A.2.2 CCE vs Track Length . . . 69
A.2.3 CCE vs Trap Concentration . . . 69
A.2.4 Electron and Hole Concentration . . . 69
A.2.5 Script (Transient) . . . 69
A.3 Strip Detector Simulations . . . 73
A.3.1 Script (Strip) . . . 73

Chapter 1

Introduction

Due to the importance and various usage of radiation in for example modern medicine, and the growing concern and consciousness around potentially harmful exposure of all kinds, the need to monitor radiation exposure is in growth, with an estimated compound annual growth rate of 6.67 % in the 2021-2026 period [1]. There should thus be room for both increased production of current products, as well as the influx of new technology to populate new niches or replacing older devices where there might be more specialised needs.

When thinking of radiation detectors one might mainly think of Geiger-Müller counters, but there are several methods or technologies used for the detection of radiation. Early methods include photographic plates, the electroscope, the spinthariscope, and cloud chambers [2]. Three major categories for radiation detectors are gas filled detectors, scintillation detectors, and solid state detectors. Gas filled detectors are based on the principle of gas in a chamber being ionised by radiation, leading to a measurable electric charge. Scintillation detectors rely on the property of certain materials to produce light when ionised by radiation, which can then further be converted to electricity, amplified and thus measured. The main principle of solid state devices are quite similar to gas filled detectors, in that the impact of radiation releases charge carriers, which then leads to a measurable current.

A rectifying metal-semiconductor junction is called a Shottky diode, where the semiconductor is typically doped with donors. In the vicinity of this junction, diffusion leads to a region stripped of free charge carriers, giving rise to the depletion region. This region grows in size by applying a reverse bias voltage. The absence of these free charges means there is an electric field in this region, set up by the ionised donors that remain. Ionising radiation causes the release of free charges where it impacts by exciting electrons to the conduction band. If this occurs in the depletion region of a diode, it will cause a flow of current across the device due to the electric field. This can then be used to detect, or measure, radiation. The most common semiconductor material

for solid state devices is silicon (Si), but the subject of this thesis is silicon carbide (SiC), or more specifically the 4H-SiC polytype. As solid state devices can be manufactured to a small size, multiple small detectors can be created close together in order to find the position of incident radiation.

Strip and pixel detectors can be made using Schottky diodes for this purpose. In a strip detector, relatively long and thin electrodes are placed on top of the semiconductor, illustrated in Fig. 1.1a. The position of incident radiation can be reduced to somewhere along a particular electrode, meaning it gives positional information in one dimension of the detector surface. While, as the name suggests, a pixel detector will have electrodes placed in a grid, illustrated in Fig. 1.1b. This means that it can be used to determine the position of incoming radiation by which electrode detected it, resulting in positional information in two dimensions of the detector surface.

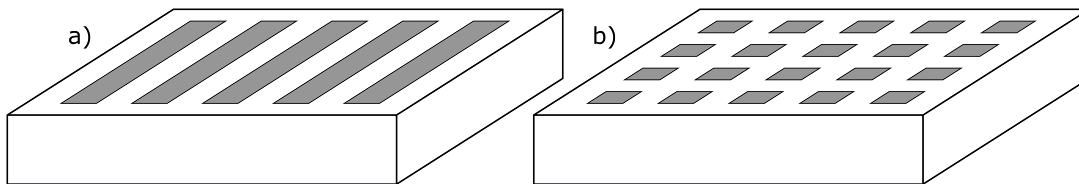

Figure 1.1: a) An illustration of a strip detector, where the strips coloured in grey indicate electrodes. b) An illustration of a pixel detector, where the square grey electrodes are placed in a grid like pattern.

The size of, and spacing between, the strip or pixel electrodes will naturally affect the resolution of the detector. One might need two separate strip detectors, or a dual sided one, in order to determine the incident position to the same degree as a pixel detector. But a pixel detector demands a much larger amount of connections to make contact to all the individual electrodes. These connections can not simply be along the surface of the device, which for example means that fixing any failed connections can be challenging [3].

A large majority of all electronic devices and components today are Si based, and although it is a relatively cheap and available material, it can unfortunately not be the most suitable for all applications. Research in other materials is aiming at further improving some aspects, like for example radiation damage. The band gap of 3.26 eV in 4H-SiC [4] is approximately 3 times larger than the band gap of 1.11 eV in Si, which means its leakage current is significantly smaller. This leads to higher temperatures and increased radiation damage having less of an impact on detector performance. Whereas an Si based detector might require cooling for it to perform to the required standard in certain applications, this might not be necessary in an SiC based detector, so it may be more suited to integration into smaller handheld or wearable devices.

This thesis will encompass the electrical characterisation of simple 4H-SiC Schottky diodes and translation of these results into numerical simulations by the Atlas software package from Silvaco Inc. These simulations aim to replicate the characteristics of the diodes after verification of their validity through comparisons with measurements. Further, the simulations are used to look at characteristics unavailable through the performed measurements. And finally, strip detectors are simulated in order to propose a viable design for a Schottky-based 4H-SiC radiation detector.

Chapter 2

Theory

As the main component of any Schottky diode is the semiconductor material, the basics of semiconductor physics and diode principles will be explained, based mainly on books by Kittel [5], Sze [6], and Streetman [7].

2.1 Semiconductor Physics

2.1.1 Fermi-Dirac Statistics

Fermi-Dirac statistics are used to explain the behaviour of certain particles, known as fermions, that have half-integer spin. This includes the electron, which is well known for its importance in electrical conduction. It can be used to describe the behaviour of electrons in solids in thermal equilibrium using the Fermi-Dirac distribution function. The function is rather simple, and describes the probability of an energy state being occupied by an electron,

$$f(E) = \frac{1}{1 + e^{\frac{E-E_F}{kT}}}, \tag{2.1.1}$$

where E is the energy in question, E_F is the Fermi level, k is Boltzmann's constant, and T is the temperature. The probability that a state is not occupied by an electron can then be written as

$$1 - f(E) = 1 - \frac{1}{1 + e^{\frac{E-E_F}{kT}}} = \frac{e^{\frac{E-E_F}{kT}}}{1 + e^{\frac{E-E_F}{kT}}} = \frac{1}{1 + e^{\frac{E_F-E}{kT}}}. \tag{2.1.2}$$

The symmetry, or rather anti-symmetry, between Eqs. 2.1.1 and 2.1.2 is here made

quite clear, and that this symmetry is centred around the Fermi level, at which the probability value is $\frac{1}{2}$ for both. An important factor to note is that at the absolute zero temperature limit, the function will be a step function, and this transition region grows larger as the temperature increases. The Fermi-Dirac distribution (Eq. 2.1.1) can be simplified if the exponential term in the denominator is much larger than one, which it will be if $E - E_F >> kT \approx 0.02585$ eV. This gives us the simplified equation

$$g(E) = \frac{1}{e^{\frac{E-E_F}{kT}}} = e^{\frac{E_F-E}{kT}}, \quad 2.1.3$$

which is used in Boltzmann statistics. The same simplification can, naturally, also be done for Eq. 2.1.2.

2.1.2 Energy Bands

The clear difference between metals, semiconductors and insulators is seen in their electrical characteristics, metals conduct electricity, insulators do not, while semiconductors are placed somewhere in between. One way to differentiate these materials is by looking at their energy bands. Energy bands are the different energy intervals at which electrons in the solid can occupy. One such band consists of a large number of energy levels that are very closely spaced, making the interval appear, and behave, as if it is continuous. The spacing between such bands in combination with the Fermi level, as seen in Fig. 2.1, is used for this differentiation between metals where the Fermi level falls well inside such a band, and semiconductors and insulators where it falls in the gap between two bands.

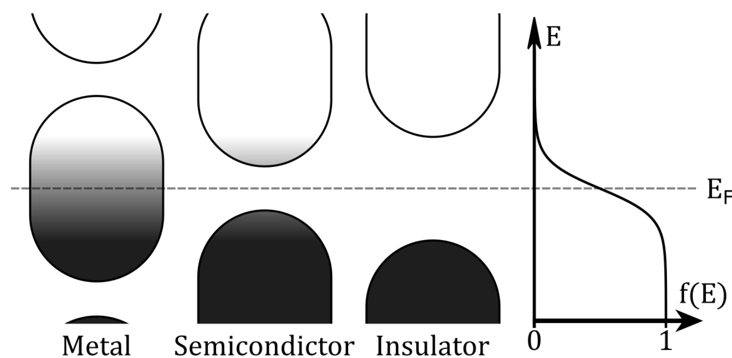

Figure 2.1: Energy band illustration of a metal, a semiconductor and an insulator. E is energy, E_F is the Fermi level, and $f(E)$ is the Fermi-Dirac distribution, signifying the probability of an energy level being occupied by an electron. The colour gradient loosely illustrates this probability, so the darkest grey means the probability is one, while completely white means that it is zero.

Although there is no definite distinction between semiconductors and insulators, the size of the band gap has traditionally been used to separate them into two categories.

In a semiconductor, the band gap is generally small enough that the available thermal energy will excite electrons from the lower to the upper energy band, respectively called the valence band and the conduction band. Meaning the resistivity of a semiconductor decreases as its temperature rises, as there will be more thermal excitation. A semiconductor is considered intrinsic if the concentration of doping, defects, and other impurities is small enough to be negligible. The Fermi level will then be in the middle of the band gap, so that the number of electrons in the conduction band will be the same as the number of holes in the valence band.

Semiconductors can be categorised by their band gap being either direct or indirect. In a direct band gap semiconductor, the highest energy state in the valence band has the same momentum as the lowest energy state in the conduction band. This means that the jump across the band gap for a charge carrier does not involve a change in momentum. Whereas in an indirect band gap semiconductor there is a momentum difference between the valence band maximum and the conduction band minimum. This difference is especially relevant for optical devices, as photons in the optical range have relatively small momenta, meaning that optical devices like LEDs and optical photodetectors are made from direct band gap semiconductors. 4H-SiC is an example of an indirect band gap semiconductor, with a band structure as seen in Fig. 2.2.

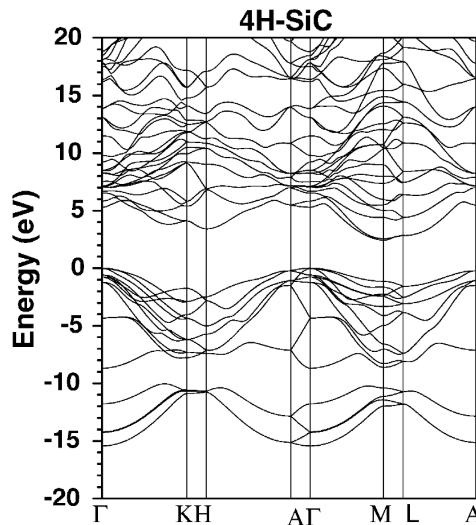

Figure 2.2: The band structure of 4H-SiC calculated with a density functional theory (DFT) based model using the local density approximation (LDA). The indirect band gap is between Γ in the valence band and M in the conduction band. Note that the size of the band gap calculated from LDA results in an underestimation, so one should not try to extract it directly from a band diagram like this. This shows a band gap of 2.43 eV, whereas it should be around 3.26 eV [4]. The figure is taken from a figure of six different polytypes in [8].

2.1.3 Charge Carriers

The significance of electrons being excited from the valence band to the conduction band lies in the fact that the electrons and the empty spaces they leave behind, named

holes, are able to carry charges in the material. Holes are treated as particles even though they do not really exist, they are essentially just the absence of an electron in the material. This also means that these quasi particles has the opposite charge of an electron, so they will also flow in the opposite direction. The way this quasiparticle moves is by an electron from another position filling in the empty space, and it will be as if the hole moved to the position the incoming electron left behind.

Charges are clearly important for the electrical characteristics of a material, as current can be defined as the flow of charged particles. The total concentration of electrons in a metal, a semiconductor, and an insulator is roughly the same, but the difference is that the electrons in an insulator are not free to flow under the influence of an electric field. Using the energy band description one can see, in Fig. 2.1, that for electrons in a metal the electrons around the Fermi level all have open slots to occupy at immediately adjacent energies, allowing them to move without significant energy needed to jump from one energy level to another.

Similarly, the electrons in the conduction band of the semiconductor are free to move and are thus contributing as negative charge carriers. While the holes in the upper part of the valence band contribute to the conductivity as positive charge carriers. These charges are thermally generated, as explained using Fermi-Dirac statistics. In a material that acts as an insulator, there will be almost no free charges generated.

The electron concentration in the conduction band at equilibrium, n_0, can be found by an integral with the help of the Fermi-Dirac distribution (Eq. 2.1.1)

$$n_0 = \int_{E_C}^{\infty} f(E)N(E)dE, \qquad 2.1.4$$

where, E_C is the energy of the conduction band edge and $N(E)$ is the density of states (DOS). Solving Eq. 2.1.4 using Boltzmann statistics, by inserting Eq. 2.1.3 will result in

$$n_0 = N_C e^{\frac{-(E_C - E_F)}{kT}}, \qquad 2.1.5$$

where N_C is the effective density of states for electrons in the conduction band, and can be written as

$$N_C = 2\left(\frac{2\pi m_n^* kT}{h^2}\right)^{\frac{3}{2}}, \qquad 2.1.6$$

where m_n^* is the effective mass of an electron at the lower edge of the conduction band, and h is Planck's constant. The same applies also to holes in the valence band at equilibrium, p_0, where the equations then are written

$$p_0 = N_V e^{\frac{-(E_F - E_V)}{kT}}, \qquad 2.1.7$$

where E_V is the energy of the valence band edge, and

$$N_V = 2\left(\frac{2\pi m_p^* kT}{h^2}\right)^{\frac{3}{2}} \qquad 2.1.8$$

is then the effective density of states for holes in the valence band, and m_p^* is the effective mass of holes at the upper edge of the valence band. The product between Eqs. 2.1.5 and 2.1.7 is

$$n_0 p_0 = N_C N_V e^{\frac{-(E_C - E_V)}{kT}} = N_C N_V e^{\frac{-E_G}{kT}}, \qquad 2.1.9$$

where $E_G = (E_C - E_V)$. Doing the same specifically for an intrinsic semiconductor gives

$$n_i p_i = N_C N_V e^{\frac{-(E_C - E_V)}{kT}} = N_C N_V e^{\frac{-E_G}{kT}}. \qquad 2.1.10$$

Further, the concentration of electrons and holes is the same for an intrinsic semiconductor, $n_i = p_i$, meaning that the intrinsic concentration of electrons can be written

$$n_i = \sqrt{N_C N_V} e^{\frac{-E_G}{2kT}}, \qquad 2.1.11$$

and the rather useful relation

$$n_0 p_0 = n_i^2, \qquad 2.1.12$$

valid at equilibrium, called the law of mass action.

2.1.4 Doping

Another helpful relation for semiconductors is charge neutrality, where positive charges in a volume is cancelled out by negative ones, such that

$$p_0 + N_d^+ = n_0 + N_a^-, \quad 2.1.13$$

where N_d^+ is the concentration of positively ionised donors, and N_a^- is the concentration of negatively ionised acceptors.

Doping of a semiconductor is used to increase the concentration of charge carriers in order to change its material properties. It is performed by introducing impurities into the material, usually in one of two forms. Dopants called donors are used to increase the concentration of free electrons in a semicondctor, making it n-doped, while acceptors are added to increase the concentration of holes, making the semiconductor p-doped. An efficient donor should have an energy level close to the conduction band when introduced in the semiconductor, so that relatively little thermal energy is needed to excite its electron. An efficient acceptor should then have an energy level close to the valence band in order to capture an electron at relatively low temperatures, and thus contribute with a hole as a charge carrier in the valence band.

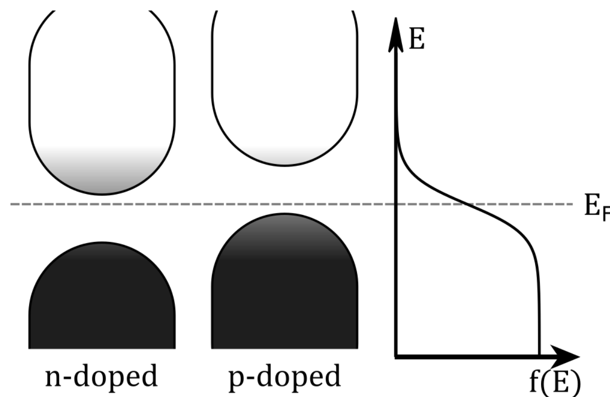

Figure 2.3: Energy band illustration of an n-doped and a p-doped semiconductor. E is energy, E_F is the Fermi level, and $f(E)$ is the Fermi-Dirac distribution, signifying the probability of an energy level being occupied by an electron. The colour gradient loosely illustrates this probability, so the darkest grey means the probability is one, while completely white means that it is zero.

In the energy band picture an n-doped semiconductor has a Fermi level in the upper half of the band gap, and using the Fermi-Dirac distribution one can from the value of the Fermi level calculate the concentration of electrons in the conduction band and holes in the valence band. In an n-doped material there will be many more electrons than holes, so the electrons are classified as majority carriers and holes as the minority

carriers. Naturally, the opposite is the case for p-doped materials. Both these cases are depicted in Fig. 2.3.

If electrons, n, and holes, p, or electron-hole pairs (EHPs), were only generated, the number of free charge carriers would always increase. So it is clear the EHPs must also be able to undergo recombination, and that a balance between generation and recombination of EHPs will be found under equilibrium or steady state conditions, where the rate of recombination, r_i, matches the rate of generation, g_i,

$$r_i = g_i. \qquad 2.1.14$$

Although these rates are dependent on temperature, for any one temperature at thermal equilibrium it can be predicted that the rate of EHP recombination, r_i, is proportional to the equilibrium concentrations of electrons, n_0, and holes, p_0 [7]. One can then write

$$r_i = \alpha_r n_0 p_0 = \alpha_r n_i^2 = g_i, \qquad 2.1.15$$

where α_r is a proportionality constant whose value depends on the particular recombination mechanism in question. A well known form of EHP recombination, called direct or band-to-band recombination, is when a photon is emitted as an electron falls from the conduction band down to the valence band to recombine with a hole. However, this is only common in direct band gap materials, as additional momentum is required for this to occur in an indirect band gap. Conversely, the generation of an EHP can occur by the absorption of an incoming photon. In an indirect semiconductor this might occur through the emission or absorption of a phonon instead of a photon.

For indirect band gap semiconductors such as Si, or 4H-SiC which is the material most relevant in this thesis, recombination occurs mainly through recombination centres or traps with energy levels within the band gap. Illustrations of Auger, trap-assisted, and band-to-band recombination can be seen in Fig. 2.4.

In the case of an n-doped material with a trap, or defect, in the band gap below the Fermi level, meaning it is likely occupied with electrons, recombination can occur as a hole is lifted from the valence band to the trap, hence opening up for an electron from the conduction band to occupy this open position at the trap level. In this process there is no net change within the trap level, while one EHP recombines, energy in the form of heat is released to the lattice in the form of vibrations, or phonons, both as the hole leaves the valence band and as the electron falls from the conduction band.

As this recombination process is more intricate than direct recombination, the lifetime of charge carriers in indirect band gap materials is also more complicated. Since this process requires that a hole is lifted to the trap level, meaning physically that an electron falls from the trap level to the valence band, it is possible that an electron in the valence band is then re-excited to the open position in the trap level before an electron in the conduction band is able to recombine with it, delaying the recombination process.

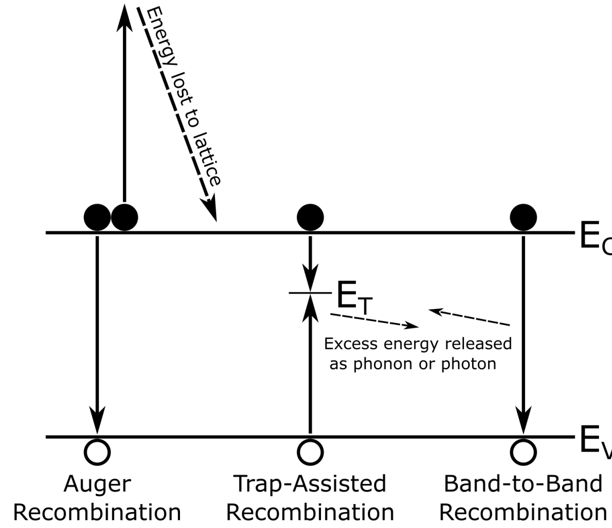

Figure 2.4: Illustrations of three common types of recombination. In Auger recombination the excess energy from the electron that falls from the conduction to the valence band goes to another electron in the conduction band, this electron then loses its excess energy to vibrations or phonons in the lattice. Trap-assisted recombination can be seen as an electron and a hole both combining at an energy trap in the band gap, coming from the conduction and the valence band, respectively. The excess energy from this process is then released as a phonon or a photon. In band-to-band recombination, an electron in the conduction band recombines with a hole in the valence band, releasing its excess energy as a phonon or a photon, with energy corresponding to the size of the band gap.

Shockley-Read-Hall (SRH) statistics can be used to describe the relationship between generation and recombination outside of an equilibrium, $n = n_0 + \Delta n$ and $p = p_0 + \Delta p$, where the excess charge carriers Δn and Δp are deviations from the equilibrium concentration. Looking at the net transition rate,

$$U = r_i - g_i, \tag{2.1.16}$$

SRH statistics gives rise to the equation [6]

$$U = \frac{\sigma_n \sigma_p v_{th} N_t (pn - n_i^2)}{\sigma_n \left[n + n_i e^{\left(\frac{E_t - E_i}{kT}\right)} \right] + \sigma_p \left[p + n_i e^{\left(\frac{E_i - E_t}{kT}\right)} \right]}, \tag{2.1.17}$$

where σ_n and σ_p is the capture cross-sections of the trap in question for electrons and holes, respectively, v_{th} is the thermal velocity, while N_t and E_t is the density and energy level of bulk traps, respectively. The net transition rate, U, is maximised for traps with an energy level equal to the intrinsic energy level. Considering only such traps, Eq. 2.1.17 simplifies to

$$U = \frac{\sigma_n \sigma_p v_{th} N_t (pn - n_i^2)}{\sigma_n (n + n_i) + \sigma_p (p + n_i)}. \tag{2.1.18}$$

Assuming low-level injection, which is when the concentration of EHPs, or excess charge carriers $\Delta p = \Delta n$, is much lower than the concentration of majority carriers, and an n-type material, gives $p = p_0 + \Delta p$ and $n \approx N_D$, where N_D is the doping concentration, so that $n_0 \gg p_0$, $\Delta p \gg p_0$, and $n_0 \gg n_i$. Using this, Eq. 2.1.18 is further simplified to

$$U \approx \frac{\sigma_n \sigma_p v_{th} N_t n \Delta p}{\sigma_n n} = \sigma_p v_{th} N_t \Delta p \equiv \frac{\Delta p}{\tau_p}, \tag{2.1.19}$$

where

$$\tau_p = \frac{1}{\sigma_p v_{th} N_t} \tag{2.1.20}$$

is the associated hole lifetime, while in a p-doped material the lifetime of an electron would then be

$$\tau_n = \frac{1}{\sigma_n v_{th} N_t}. \tag{2.1.21}$$

For high-level injection, meaning that the concentration of excess charge carriers is much larger than the doping concentration, $\Delta p = \Delta n \gg n_0$, the lifetime for electrons and holes is equal, and given by

$$\tau_n = \tau_p = \frac{\sigma_n + \sigma_p}{\sigma_n \sigma_p v_{th} N_t} = \frac{1}{\sigma_n v_{th} N_t} + \frac{1}{\sigma_p v_{th} N_t}, \tag{2.1.22}$$

found by inserting the high-level injection condition into Eq. 2.1.18. Showing that the lifetime increases with higher injection levels, which is opposite to the behaviour of band-to-band recombination [6].

2.1.5 Carrier Mobility

The ease at which a charge carrier can move, or drift, in a material is given by its mobility, μ, or μ_n for electrons and μ_p for holes. At low electric fields, given electrons as the charge carrier, its relation to the conductivity can be written

$$\sigma_n = qn\mu_{0,n}, \tag{2.1.23}$$

where q is the elementary charge and n is the electron density. Further, the value of the mobility can be calculated from the average time between collisions for the charge carrier in the material, called the mean free time, $\bar{t}$, the effective mass of the charge carrier, m^*, and again the elementary charge by the equation [7]:

$$\mu = \frac{q\bar{t}}{m^*}, \tag{2.1.24}$$

where a subscript of n or p can be used for the mobility and effective mass to differentiate between electrons and holes, respectively. The conductivity of a material with both electrons and holes as contributing charge carriers simply becomes

$$\sigma = q\left(n\mu_{0,n} + p\mu_{0,p}\right). \tag{2.1.25}$$

The mean free time of a particle is affected by collisions, which is mainly dependent on temperature and impurities through lattice scattering and impurity scattering, respectively. Higher temperatures means there are more vibrations, or phonons, in the lattice which increases the probability of collisions. While for low temperatures, where lattice collisions might be neglected, interactions with charged defects cause mobility to decrease with the temperature as slower carriers interact more strongly with charged defects at slower speeds [7]. Meaning that both doping concentration and unwanted defects will decrease the mobility in a material. The effect from multiple scattering mechanisms on mobility can be summed together using Matthiessen's rule, which means adding together the inverse of the individual contributions,

$$\frac{1}{\mu} = \sum_i \frac{1}{\mu_i}. \tag{2.1.26}$$

The temperature dependence of the mobility contribution related to lattice scattering is $\mu_l \propto T^{-3/2}$, while for impurity scattering it is $\mu_i \propto T^{3/2}$ [6], so when these mechanisms are the two dominant contributors, the temperature dependent mobility can be

written

$$\mu(T) = \left(\frac{1}{\mu_l} + \frac{1}{\mu_i}\right)^{-1} = \left(\frac{k_l}{T^{3/2}} + \frac{k_i}{T^{-3/2}}\right)^{-1}, \tag{2.1.27}$$

where k_l and k_i are temperature independent constants for the lattice and impurity related mobility terms, respectively. A logarithmic plot of this can be seen in Fig. 2.5, where the individual terms relating to impurity scattering and to lattice scattering is plotted as dotted lines, forming an upper bound of the total mobility.

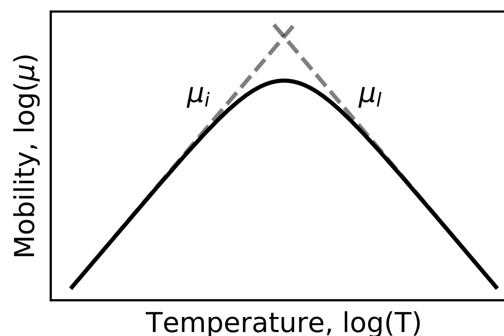

Figure 2.5: A simple plot of the temperature dependency of mobility when accounting for lattice and impurity scattering, with respective temperature dependencies of $T^{-3/2}$ and $T^{3/2}$.

2.2 Diodes

The simplest idea, or approximation, of a diode is that it conducts current in one direction and opposes it in the other direction. This means there is low resistance in one direction, and high resistance in the other. The range of applications for semiconductor diodes is immense, from solar panels to transistors (computers) and LEDs. But here the focus will be on the physics in the junction between n- and p-doped semiconductors, and the junction between an n-doped semiconductor and a metal, a Schottky diode.

Diodes are called rectifying due to the non-linear relationship between current and applied voltage. In the reverse direction, meaning when the applied potential is negative, the current is limited by the reverse saturation current, while in the forward direction the current increases exponentially as a function of voltage. In reality, ohmic resistance will naturally limit the current in the forward direction, while in the reverse direction, as the potential grows large enough, some sort of breakdown will occur, where the reverse current will increase sharply in the negative direction. Zener breakdown is usually the cause of breakdown in diodes of highly doped materials, where

at relatively low voltages, the energy bands are close enough for electrons to easily tunnel through. For more lightly doped materials, Avalanche breakdown occurs at higher voltages, where electrons are accelerated by the electric field to such energies that they can excite electrons they interact with to the conduction band. This leads to a chain reaction, and thus a drastic increase in free electrons, causing a sharp reduction in resistance and hence also a sharp increase in reverse current.

2.2.1 P-N Junctions

Given an abrupt transition between two areas with different doping concentrations, diffusion will cause a flow of carriers against the concentration gradient. So with a junction between an n-doped and a p-doped material, electrons will begin to flow from the n-doped region into the p-doped region, while holes will move in the opposite direction. This leaves a region around the junction depleted of charge carriers, where the stationary ions are left behind. This sets up an electric field, from the n-side (positive ions) to the p-side (negative ions), which in turn affects the flow of charge carriers, contributing to a drift in the opposite direction of the diffusion flow. This naturally leads to an equilibrium between carrier flow caused by the concentration gradient and the electric field, and a resulting built-in potential V_0. The depletion region between the two areas has a width equal to [6]

$$W_{pn} = \sqrt{\frac{2\varepsilon_s(V_0 - V - \frac{2kT}{q})}{q}\left(\frac{1}{N_a} + \frac{1}{N_d}\right)}, \quad 2.2.1$$

where ε_s is the permittivity of the semiconductor, V is applied voltage, and the term $2kT/q$ accounts for a contribution by the majority-carriers on each side of the junction [6]. Due to charge neutrality of the junction as a whole, the number of positive ions in the n-region must equal the number of negative ions in the p-region. With help of the doping concentrations, the size of the depletion region located on the n-side and the p-side of the junction is

$$W_n = W_{pn}\frac{N_a}{N_a + N_d} \quad 2.2.2$$

and

$$W_p = W_{pn}\frac{N_d}{N_a + N_d} \quad 2.2.3$$

respectively. A diagram of the energy band across a junction where the doing concentration is equal on both sides can be seen with and without an applied bias in Figs. 2.6a and 2.6b, respectively.

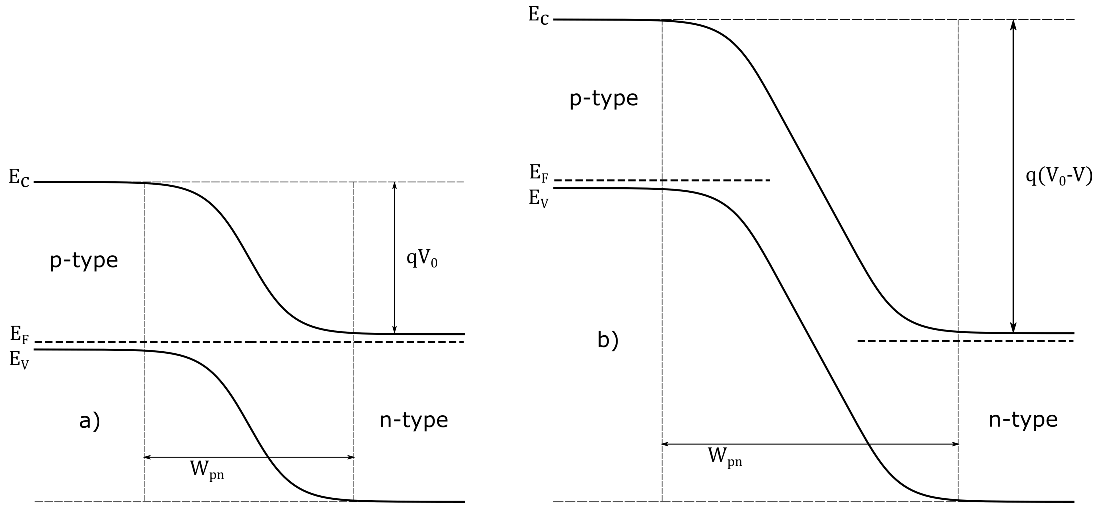

Figure 2.6: a) An energy band diagram across a pn-junction in equilibrium. b) A steady-state energy band diagram across a pn-junction with an applied reverse bias. A tentative visualisation of the width of the depletion region W_{pn} can be seen for both cases, and is increased by a reverse bias.

The current through a diode as a function of the potential across it is given by the Shockley diode equation [7]

$$I = qA\left(\frac{D_p}{L_p}p_n + \frac{D_n}{L_n}n_p\right)\left(e^{\frac{qV}{kT}} - 1\right) = I_0\left(e^{\frac{qV}{kT}} - 1\right), \quad 2.2.4$$

where A is the area of the diode, D_n and D_p is the diffusion coefficients for electron and holes, respectively, L_n and L_p is the diffusion lengths for electrons and holes, respectively, p_n is the concentration of holes in the n-doped region, n_p is the concentration of electrons in the p-doped region, and I_0 is the reverse saturation current. The depletion region is reduced as forward voltage increases, while it is expanded with the increase of reverse voltage.

2.2.2 Schottky Diodes

A metal-semiconductor junction will either form an ohmic contact or a rectifying Schottky barrier, mainly dependent on the height of the Schottky barrier that is formed by the junction. In the ideal case, it is

$$\Phi_B = \phi_M - \chi, \quad 2.2.5$$

where ϕ_M is the work function of the metal and χ is the electron affinity of the semiconductor. The width of the depletion region for a Schottky diode is written slightly simpler than for a pn-junction, as the p-doped region is replaced with metal, meaning that the entire depletion region will lie in the n-doped semiconductor, and is thus given by

$$W_{Sc} = \sqrt{\frac{2\varepsilon_s(V_0 - V - \frac{kT}{q})}{qN_d}}, \qquad 2.2.6$$

where the factor kT/q is not multiplied with a factor 2 as it was for a pn-junction, since there is only one semiconductor side in a metal-semiconductor junction, and thus there will only be one instance of a charge carrier distribution tail. According to thermionic-emission-diffusion (TED) theory [6], the ideal Schottky diode equation is given by

$$I = A^{**}T^2 e^{-\frac{q\Phi_B}{kT}} \left(e^{\frac{qV}{kT}} - 1\right) = I_0 \left(e^{\frac{qV}{kT}} - 1\right), \qquad 2.2.7$$

where A^{**} is the effective Richardson constant for TED.

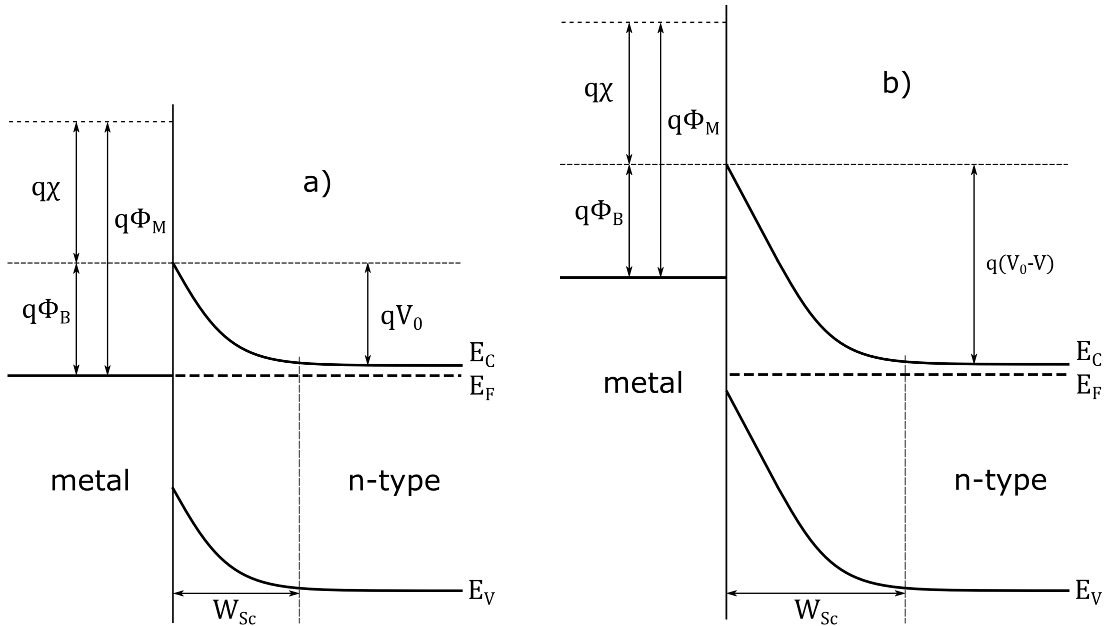

Figure 2.7: a) An energy band diagram across a Schottky diode in equilibrium. b) A steady-state energy band diagram across the same Schottky diode under the influence of an applied reverse bias. A tentative visualisation of the width of the depletion region W_{Sc} can be seen for both cases, and is increased by a reverse bias.

Illustrations of an energy band diagram for a Schottky diode with and without applied reverse bias can be seen in Figs. 2.7a and 2.7b, respectively, where the barrier height is

visualised on the left hand side of both illustration. One can also see how the energy band of the n-type semiconductor is shifted down relative to the metal side as a reverse bias is applied, as well as the growth of the depletion region.

One should keep in mind that the work function of the metal and the electron affinity of the semiconductor can not be said to always be the dominant factors for barrier height. In many metal-semiconductor junctions it is instead caused by defect states on the interface in the form of Fermi level pinning [9] [10].

2.2.3 Diode-Based Detectors

Particles, including photons, with enough energy are able to knock electrons from the valence to the conduction band. Such ionising radiation can be detected as it enters the depletion region of a semiconductor junction, as the release of EHPs in its electric field would result in a spike of current through it. In controlled conditions this can be used as a reliable method for detection of ionising radiation, the amount of charge released by the radiation can be found from integrating the current over time. From this, the energy of the impacting radiation can be found by comparing this charge with the energy needed to create EHPs in the material. The location of the incoming radiation might demand multiple diodes in a strip or pixel configuration on a microscopic scale, depending on the required resolution.

Chapter 3

Experimental Methods and Details

The basis for the experimental part of this work is a sample of an n-doped 4H-SiC wafer with a 10 µm thick epitaxially grown layer, with a 1 µm buffer layer in between. From the fabrication specifications, the donor concentration of the epitaxial layer is about $1 \cdot 10^{15}$ cm $^{-3}$, the buffer layer has a concentration of $1 \cdot 10^{18}$ cm^{-3}, while the concentration in the substrate is approximately $3 \cdot 10^{18}$ cm^{-3}. The sample consists of 16 Schottky diodes with circular nickel electrodes, all with a thickness of 150 nm and a diameter of 1 mm, with an estimated uncertainty of 5%. An illustration of the semiconductor stack, including two circular top electrodes can be seen in Fig. 3.1. The experimental work consists of performing I-V, C-V, and DLTS measurements on this sample.

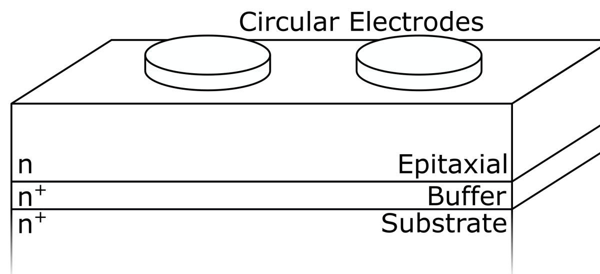

Figure 3.1: An illustration of the physical device upon which measurements were performed. Two circular electrodes are included in the illustration, and can be seen to lie on top of the epitaxial layer. Beneath the n-doped epitaxial layer is a thin, heavily doped, buffer layer, and at the bottom is the thick substrate, which is also heavily doped.

3.1 Current-Voltage (I-V) Measurements

Fabricated diodes can be of varying quality. Owing to this, an ideality factor is often included in an ideal diode equation to quantify how closely the I-V characteristics of a diode follows the ideal case. For a Schottky diode, this would mean Eq. 2.2.7 can be rewritten as

$$I = I_0 \left(e^{\frac{qV}{\eta kT}} - 1 \right), \quad 3.1.1$$

where η is the ideality factor, with a value that generally lies somewhere between 1 and 2, where a value of 1 corresponds to an ideal diode.

3.2 Capacitance-Voltage (C-V) Measurements

The built-in potential and the doping concentration can be found with the help of capacitance measurements as a function of applied potential. The capacitance over the junction will be

$$C = \frac{\epsilon_s A}{W}, \quad 3.2.1$$

where A is the diode area. With a semiconductor of a constant doping concentration, the depletion width, W_{Sc}, from Eq. 2.2.6 can then be inserted into Eq. 3.2.1, then squaring and inverting the equation so that

$$\frac{1}{C^2} = \frac{2(V_0 - V - \frac{kT}{q})}{qA^2\varepsilon_s N_d}. \quad 3.2.2$$

Were one to differentiate Eq. 3.2.2 with regards to V, one would get

$$\frac{d\left(1/C^2\right)}{dV} = -\frac{2}{qA^2\varepsilon_s N_d}. \quad 3.2.3$$

Both Eqs. 3.2.2 and 3.2.3 make it apparent that a plot of $1/C^2$ versus V results in a straight line, for a constant doping profile. However, for an arbitrary doping constant, Eq. 3.2.3 would instead look like [6]

$$\frac{d\left(1/C^2\right)}{dV} = -\frac{2}{qA^2\varepsilon_s N_d(x)}, \quad 3.2.4$$

where x is the depth into the junction.

The inverse of the square capacitance was fitted to Eq. 3.2.2 using linear regression. Both the slope, a, and intercept, b, from this fitting was then used to calculate the

built-in voltage,

$$V_0 = \frac{kT}{q} - \frac{b}{a}, \tag{3.2.5}$$

and the donor concentration,

$$N_d = \frac{-2}{q\epsilon_s A^2 a}. \tag{3.2.6}$$

3.3 Deep-Level Transient Spectroscopy (DLTS)

DLTS is a capacitance spectroscopy-based technique for rectifying junctions that is used for detecting defects with energy levels in the band gap. Being "deep level" defects refers to their energy levels being more to the middle of the band gap than is required for traditional dopants, and are generally undesirable as they can substantially reduce the lifetime of charge carriers [6]. The capacitance in the junction of a rectifying diode is dependent on charged defects in the depletion region mainly in the form of ionised dopants, though in DLTS the capacitance caused by deep level traps is utilised. The diode is set to a fixed reverse bias, which is briefly upset by a short reduction in absolute voltage, resulting in a similar pulse for the capacitance in accordance with Eq. 3.2.2. However, the new voltage across the diode also leads to deep level traps close to the junction being occupied, causing a decrease in capacitance. After the reverse bias is again increased, these traps do not immediately become unoccupied, but rather there is an emission rate for electrons and holes given by [11]

$$e_n = \sigma_n \langle v_n \rangle_{th} N_C e^{-\frac{E_C - E_t}{kT}} \tag{3.3.1}$$

and

$$e_p = \sigma_p \langle v_p \rangle_{th} N_V e^{-\frac{E_t - E_V}{kT}} \tag{3.3.2}$$

respectively, with units s^{-1}, where σ is the capture cross-section, $\langle v \rangle_{th}$ is the average thermal velocity, E_t is the energy level of the trap, N_C and N_V is the effective density of states in the conduction and valence band, respectively, and E_C and E_V is the energy level of these respective bands. The exponential pre-factors in the emission rates are proportional to the square of the temperature, $e_n, e_p \propto T^2$, as the thermal velocity

is proportional to the root of temperature, $\langle v \rangle_{th} \propto T^{1/2}$, and the effective density of states is proportional to temperature to the power of three halves, $N_C, N_V \propto T^{3/2}$, as seen in Eqs. 2.1.6 and 2.1.8. This temperature dependency means that Eq. 3.3.1 can be written as

$$\ln\left(\frac{e_n}{T^2}\right) = -\frac{\Delta E_t}{k}\frac{1}{T} + \ln\left(\sigma_n K_n\right), \tag{3.3.3}$$

where $K_n = \langle v_n \rangle_{th} N_C / T^2$ is a temperature-independent constant and ΔE_t is the energy level of the trap with respect to the conduction band.

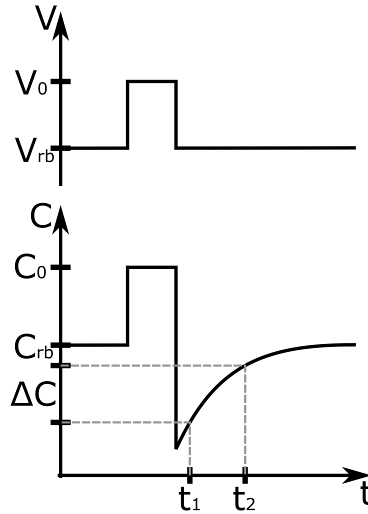

Figure 3.2: An illustration of the capacitance over time, and its response to a voltage pulse. The capacitance has changed ΔC from $t = t_1$ to $t = t_2$. V_{rb} and C_{rb} is the reverse bias steady state value for the voltage and capacitance, respectively, while V_0 and C_0 is the voltage and capacitance during the pulse, respectively.

Going forward, the focus will be on emitting traps, or acceptors, so $e_n \gg e_p$. Given that the voltage pulse is sufficiently long the concentration of occupied traps, $\mathcal{N}_t(0)$, will be equal to the trap concentration, N_t. Over time, the occupied trap concentration will decrease exponentially in accordance with [11]

$$\mathcal{N}_t(t) = N_t e^{-e_n t}, \tag{3.3.4}$$

leading to a similar response for the capacitance, as illustrated in Fig. 3.2,

$$C = C_{rb} - C_{rb}\frac{N_t}{2N_t}e^{-e_n t}, \tag{3.3.5}$$

where C_{rb} is the steady state reverse bias capacitance, to which the capacitance returns as the electrons are emitted from the traps. One of the approaches to determine the

emission rate is by sampling the capacitance at fixed time intervals (Fig. 3.2). This is the so-called boxcar method. Using the difference in capacitance between these one can calculate the temperature dependent DLTS signal

$$S(T) = \Delta C \left(e^{-t_1/\tau} - e^{-t_2/\tau} \right), \qquad 3.3.6$$

where t_1 is the time of the first sampling and t_2 is then the time of the second. The maximum of this signal (Eq. 3.3.6) for a given sampling time interval is found at

$$\tau_{max} = (t_1 - t_2) \ln \left(\frac{t_1}{t_2} \right) = t_1 (x - 1) \ln(x), \qquad 3.3.7$$

where $x = t_2/t_1$, which can then be inserted back into Eq. 3.3.6 to give its maximum

$$S_{max} = \Delta C \left(e^{-\frac{\ln x}{x-1}} - e^{-\frac{x \ln x}{x-1}} \right) = \Delta C \cdot F. \qquad 3.3.8$$

Further, the trap concentration is related to the DLTS signal through

$$\frac{N_t}{N_d} = \frac{2\Delta C}{C_{rb}}, \qquad 3.3.9$$

where N_t is the trap concentration, N_d is the donor concentration, and ΔC is the capacitance difference between the two points in time. Meaning that the peak heights of the measured DLTS signal can be used to calculate its respective trap concentration.

Another approach for deducing the DLTS signal less sensitive to noise is the lock-in method. Rather than only using two capacitance values, capacitance measured over a time window, t_i, and multiplying with a sampling function, $\omega(t)$ (Fig. 3.3). The integral over the first half of the time window is subtracted by the integral over the second half. The DLTS signal can then be written [12]

$$S(t_i) = \frac{1}{t_i} \int_{t_d}^{t_d + t_i} \Delta C(t) \omega(t) dt, \qquad 3.3.10$$

where t_d is the delay between the pulse and the start of the measurement window, t_i, is the duration of this window, $\Delta C(t) = C_{rb} - C(t)$ is the capacitance relative to the reverse bias capacitance, and

$$\omega(t) = \begin{cases} +1, & t_d \leq t \leq t_d + \frac{t_i}{2} \\ -1, & t_d + \frac{t_i}{2} < t \leq t_d + t_i \end{cases}, \qquad 3.3.11$$

is the sampling function. The six time intervals used during the DLTS procedure are stated in Table 3.1, which also displays further values needed to calculate the trap concentration, based on a setup using the lock-in approach.

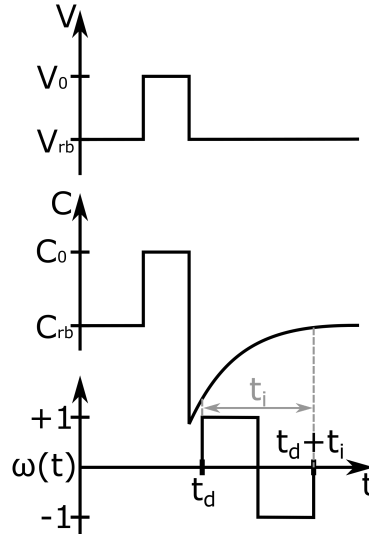

Figure 3.3: An illustration of the capacitance during DLTS using the lock-in approach. A voltage pulse is applied, influencing the capacitance. The DLTS signal is found by subtracting the integral over the first half of the measurement window with the integral over the second half.

Table 3.1: A list of parameters used when extracting data from the DLTS measurements, specific to the utilised measurement setup, using the lock-in approach. τ is the length of the time interval, e_n is the emission rate for electrons used in Eq. 3.3.1, F is the value used for the constant in Eq. 3.3.8, and i is the time interval in question. All these values are taken directly from an in-house document, relating to the specific measurement station used.

i	τ_i [ms]	$e_{n,i}$ [s^{-1}]	$F_i = S_{max}/\Delta C$
1	20	72.448	0.1025
2	40	45.429	0.1387
3	80	26.225	0.1672
4	160	14.264	0.1851
5	320	7.471	0.1946
6	640	3.828	0.1993

3.4 Experimental Details

The electrical measurements were all performed on the measurement station seen in Fig. 3.4, where electrical contact is made on a chosen electrode through the needle which also serves to keep the sample in place. Silver paste applied to the backside of the sample leads to an electrical connection to the plate on which it is clamped, closing the circuit to allow for measurements on the diode in question. A lid is also put in place to cover the sample from light, or photons, during measurements.

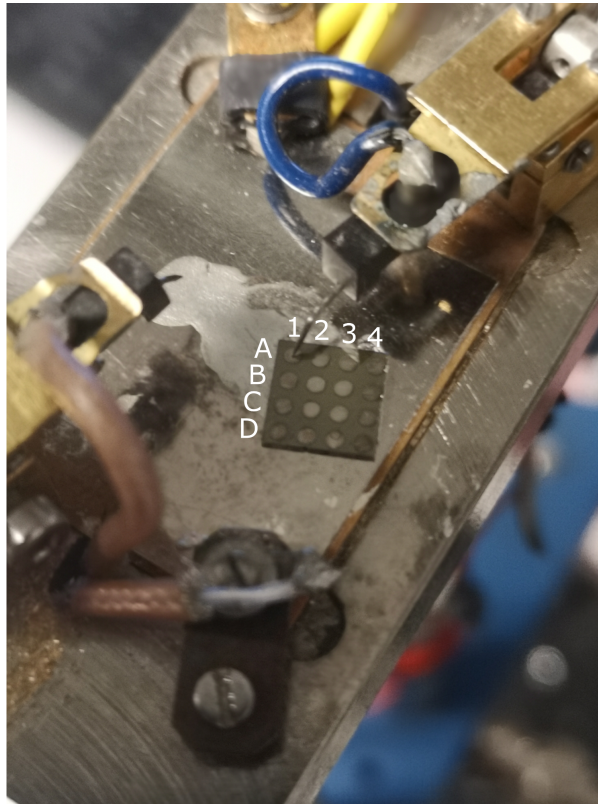

Figure 3.4: A picture of the measurement station and the sample used with 16 Schottky diodes, including the labelling scheme used to differentiate between them. For scale, the circular nickel electrodes have a diameter of 1 mm.

The current-voltage characteristics for four of the 16 Schottky diodes in the aforementioned sample was measured for voltages between 1 and -1 V, with voltage steps of 0.05 V, using a Keithley K617 electrometer. The lower detection limit of the Keithley 6487 picoammeter is $4 \cdot 10^{-13}$ A, or 0.4 pA. The maximum available voltage range of the measurement setup was ± 10 V, but voltages below -1 V are excluded as the leakage currents of the devices are well below its measurement limit, while no measurements were performed above 1 V.

The capacitance was also measured as a function of voltage using the same measurement station, and a HP 4280A capacitance meter. This measurement was performed

on a single Schottky diode, for voltages between 0 and -10 V with intervals of 0.25 V, where -10 V was the lowest available voltage. A linear regression of Eq. 3.2.2 is performed, and its slope and intercept used to calculate the built-in voltage and doping concentration in the diode.

The same measurement station was used for DLTS measurements. In order to vary the temperature, the sample holder was lowered into liquid nitrogen. The procedure was started when the temperature had cooled to below 83 K. A heater was then used to increase the temperature, and the measurement was automatically repeated for every degree between 83 K and 350 K. The temperature measurements were perfomed by a Keithley 2700 multimeter, and the HP 8112A was responsible for pulse generation.

Chapter 4

Simulations

In order to further corroborate the electrical properties of the Schottky diode, as well as predict its performance as a radiation detector, numerical simulations were conducted. For this purpose, the numerical device simulation software Atlas [13] was used through the Deckbuild interface, both products of Silvaco Inc.

4.1 Single Diode Simulations

The final goal is to simulate a Schottky based detector that can detect the energy and location of ionising radiation. One stand-alone Schottky diode should be able to detect when it is irradiated, but without providing accurate information about the incidence point of the radiation on the device. One should, however, be able to calculate the amount of radiation through integrating the current over time as radiation releases charge carriers within its depletion region. A pseudo one dimensional (1D) computer model was constructed, and verification of its validity was done though comparison to the measurements. It was used to investigate properties and perform tests that are not as easy to do in experimental tests. The illustration of the 1D model showing the different layers of the simulated structure can be seen in Fig. 4.1.

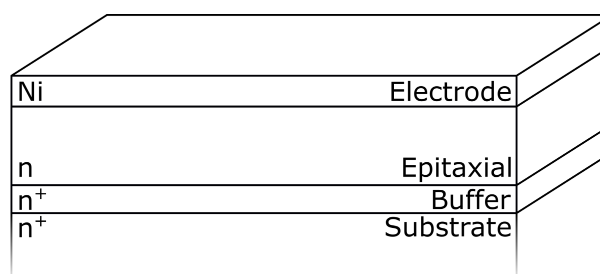

Figure 4.1: An illustration of the simulated single electrode diode, which has a 1D structure. The electrode, which in the simulations has no physical thickness, is placed on top of the epitaxial layer. Beneath the n-doped epitaxial layer is a thin, heavily doped, buffer layer, and at the bottom is the thick substrate, with a doping concentration similar to the buffer layer.

An essential part for receiving reliable simulation results is the spatial resolution of the points used in the simulation, referred to as the meshgrid. The number of mesh points in a numerical simulation dictates both the accuracy and the computational load. As such, a compromise must be found between execution time and result accuracy. The resolution of the grid was increased around junctions and other points of interest, like the impacting electron for the later transient simulations. It is important that the grid resolution is set high enough to achieve convergent results. Another detail that proved important for the SiC simulations was using 128 bit, rather than the default 64 bit, due to the low current seen in high band gap materials being more sensitive to the resolution in the floating point numbers, compared to a semiconductor like silicon.

By implementing the measured parameters in the software, simulations could be performed in order to compare to experimental data. To simulate simple I-V measurements, start, stop and step voltages corresponding to the physical measurements were implemented by defining them in the **solve** statement. The current as a function of voltage was then extracted from the resulting file by choosing the right columns for the respective values. As with the measured I-V curves, these data were also fitted to the diode equation (Eq. 3.1.1), giving an ideality factor and estimated reverse saturation current.

Although measurements of the I-V characteristics at large reverse biasas could not be performed due to the limitation in the voltage range of the instrument, these conditions could be simulated. This was done by including models for impact ionisation and band-to-band tunnelling, and simulating for reverse voltages up to 1650 V.

The capacitance as a function of the applied potential was also simulated, again to do a comparison with the measurements. The same linear fit of Eq. 3.2.2 was then performed on the same voltage range as the measured data, from which the doping concentration and reverse current was calculated to complete the comparison. When calculating the capacitance, the arguments *qscv* (quasistatic capacitance) and *nocurrent* were included in the **solve** statement to calculate the capacitance and to reduce simulation time, respectively. The model *bgn.lind* was not included in simulations of capacitance, as the simulations did not seem to converge when it was enabled.

The reverse bias voltage was then increased beyond the range available for physical measurements, and the plot of the capacitance as the reverse bias increased to 500 V was used to determine the voltage needed to reach complete depletion of the epitaxial layer by identifying where the capacitance saturates. This is useful in determining what potential is needed to obtain complete collection of eventual free charge carriers

released in the epitaxial layer by, for example, radiation.

4.2 Transient Simulation

To predict the effect of an energetic particle hitting the device, a track of released EHPs was added to simulate an incident particle, using the **singleeventupset** statement. It was set to release a charge concentration of 80 $q/\mu m$ along its path. This type of particle is known as a minimum ionising particle (MIP), and can be thought of as a high energy electron or proton. To set up these simulations, the voltage was first ramped up to the desired value, leaving the device in a steady state with a given potential and electric field in the epitaxial layer. Time dependent, or transient, simulations can then be performed over the desired temporal range to see the result of the impacting particle. The transient simulations were set to last for 10 ns. The integrated collected charge was then compared to the total charge induced by the particle.

To deduce the charge collection efficiency (CCE), the amount of collected charge can be calculated as a fraction of the charges released in the epitaxial layer. This could then be compared with the total charge released along the track, to determine how completely the device might collect charges released by radiation. Due to the high doping in the buffer layer and in the substrate the depletion region will not encompass these regions, leading to a much smaller electric field, so charges in those areas are expected to recombine before being collected. The expected amount of collected charge obtained from the integration are thus only from those released inside the 10 µm thickness of the epitaxial layer. With a 80 $q/\mu m$ charge concentration along the track, this amounts to 800 q for all simulations except where the track does not penetrate the entire epitaxial layer.

For these simulations, the particle track was in the centre of the device and kept vertical. The meshgrid was fine-tuned horizontally around the centre and edges of the track, making these transient simulations two dimensional (2D) in nature, but with the electrode still covering the entire top layer. Reverse bias voltages of 0, 25, 50, 100, 250, and 500 V were tested in the transient simulations to determine the impact of biasing on CCE. To verify whether the charges released in buffer layer and in the substrate contributed to CCE, or underwent recombination too quickly to noticeably impact the current, different track lengths were also tested. The track lengths tested were 2, 4, 6, 8, 10, and 12 µm, focusing on tracks within the epitaxial layer, with only the longest one going beyond it.

The effect of the traps discovered from the DLTS procedure was investigated by including the $Z_{1/2}$ trap in the simulations, by the use of the **trap** statement, using the parameters found; energy level, electron capture cross section, and concentration. The hole capture cross section was set equal to the value found for electrons, and the degeneracy level was set to 1. In an effort to determine how detrimental this trap could be to the characteristics of the device, concentrations ranging from 10^{13} up to 10^{20} cm^{-3} were tested for the transient simulations.

In order to visualise the movement of charge carriers in the device with a reverse bias of 500 V, and a track penetrating the entire device, the simulated values at every grid point was saved at each time step. To represent the time evolution of the electrons and holes, distributions of electron and hole concentrations were plotted side by side, for selected time steps.

4.3 Strip Detector Simulations

Multiple electrode models were created in the same software to investigate a microstrip detector design, which would have the purpose of detecting the location of incoming radiation with increased accuracy. The electrodes in a microstrip design are placed like the teeth of a comb. By doing readings from the individual electrodes, the position of incident radiation can be determined in one dimension. The inclusion of an identical device rotated 90° can be used to pinpoint the exact location in two dimensions.

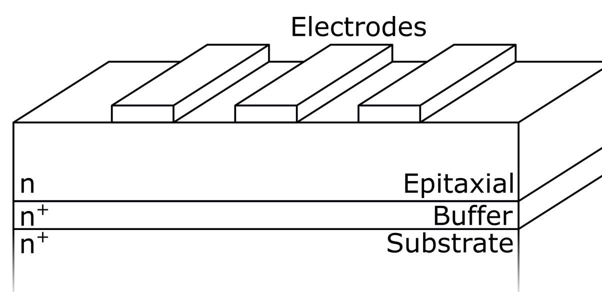

Figure 4.2: An illustration of the simulated strip detector design. Three finger electrodes are placed on top of the epitaxial layer. Beneath the n-doped epitaxial layer is a thin, heavily doped, buffer layer, and at the bottom is the thick substrate, with a doping concentration similar to the buffer layer.

The implementation of the strip model into the simulation software was done by including 3 top electrodes, or fingers, as illustrated in Fig. 4.2. The widths of and the spacings between the electrodes were set equal, using three different designs by setting them to 10, 20, and 30 µm. The potential field set up by the individual electrodes

by the applied voltage must be expansive enough to also extend laterally to fill the epitaxial layer in the space between them, so that radiation in between the electrodes is also detected. This leads to a necessary balance between the strength of applied voltage and spacing between electrodes, as larger applied voltages are needed to fill a larger gap.

To incorporate the microstrip design, separate electrode and contact statements are made for each electrode, and the resolution of the meshgrid in the x-direction is especially increased around the edges of the electrodes, but also within the electrode and in the space between them. Additionally, the meshgrid is fine-tuned around the radiation track for its different impact position. In order to find a desirable design for the microstrip detector, the collected charge from each individual electrode was calculated as the position of the vertical track was scanned across two neighbouring strips, mapping the charge collection for different designs and applied voltages. Two different designs were tested with reverse bias voltages of 100, 200, and 400 V, one had widths and spacing between the electrode fingers of 10 µm, while the other had widths and spacings of 20 µm. Additionally, a design with widths and spacings of 30 µm was tested using only 400 V.

4.4 Physical Models

With the exception of quantum computers which currently may simulate a system of just over 100 particles [14], approximations and generalisations have to be made in order to model parts of the real world. One very famous example of this is Newton's law of universal gravitation, which as a model of gravitation works remarkably well in explaining observable effects of gravitation. However, as is often the case with models, it fails at explaining observations far from range of observations from which it was developed, like the magnitude of deflection for light rays passing by a massive body [15].

The thicknesses and doping concentrations of the three layers in the semiconductor structure is listed in Table 4.1. Since the physical diode consists of 4H-SiC, the semiconductor material is all modelled as 4H-SiC, where the properties used in the **material** statement to model it is taken from an example file from Silvaco [16], which uses [17] as reference. The material properties relating to the semiconductor mobility are given in a separate **mobility** statement, needed for the implemented mobility models. The impact ionisation and band-to-band parameters, used only when looking at the reverse bias breakdown, were also extracted from the same example code.

Table 4.1: A list of the thickness and doping concentrations of the three different layers in the semiconductor stack. The concentration in the epitaxial layer is found through the previous capacitance measurements, while the other values are from manufacture specification. With exception of the substrate thickness, which has its thickness greatly reduced to 30 µm in the simulations.

	Thickness [µm]	Doping Concentration [cm^{-3}]
Epitaxial Layer	10	$1.134 \cdot 10^{15}$
Buffer Layer	1	$1 \cdot 10^{18}$
Substrate	30	$3 \cdot 10^{18}$

4.4.1 Mobility

An empirically derived hyperbolic model for carrier mobility as a function of doping concentration and temperature is given by Caughey and Thomas in [18]

$$\mu_0 = \mu_{min} + \frac{\mu_{max} - \mu_{min}}{1 + \left(\frac{N}{N_{ref}}\right)^{\alpha}}, \qquad 4.4.1$$

which can be applied both to electrons and holes, where μ_0 is the low field mobility as a function of doping concentration, N, while μ_{min} corresponds to the mobility of the given material at very high doping concentration, μ_{max} equals the higher mobility found for undoped samples, N_{ref} is the doping concentration required to give a mobility halfway between μ_{min} and μ_{max}, and α is a parameter that helps in fitting to how fast the mobility changes between μ_{min} and μ_{max} as a function of N. Further, this equation can be expanded to include temperature dependence by making the μ_{min}, μ_{max}, N_{ref}, and α parameters temperature dependent in accordance with [19]

$$Par = Par_0 \left(\frac{T}{300\ \text{K}}\right)^{\gamma_{Par}}, \qquad 4.4.2$$

where Par is the parameter in question, Par_0 is the value of that parameter at room temperature, T is the temperature, the denominator shows the reference/room temperature of 300 K, and γ_{Par} is a fitting parameter for that specific parameter.

Lastly, at high electric fields the mobility is reduced as the charge carriers reach their saturation velocity, unable to keep speeding up as the potential increases. Using experimental data from silicon, an electric field dependent relation for carrier mobility was also obtained by Caughey and Thomas [18], which is the model implemented in the simulation software Atlas [13]. For electrons it is written

$$\mu_n(E) = \mu_{0,n} \left(\frac{1}{1 + \left(\frac{\mu_{0,n} E}{v_{s,n}} \right)^{\beta_n}} \right)^{\frac{1}{\beta_n}}, \quad 4.4.3$$

where E is the electric field, v_s is the saturation velocity of the carrier, β is an experimentally determined constant, and the subscript n is still used to signify that the respective value corresponds to electrons as the charge carrier. In [18] the values of β for silicon semiconductors were deemed to be $\beta_n = 1$ and $\beta_p = 2$. The mobility of holes is then similarly written

$$\mu_p(E) = \mu_{0,p} \left(\frac{1}{1 + \left(\frac{\mu_{0,p} E}{v_{s,p}} \right)^{\beta_p}} \right)^{\frac{1}{\beta_p}}. \quad 4.4.4$$

In order to model the mobility of charge carriers in the semiconductor, the analytic low-field mobility model [13] was utilised, using the model parameter *analytic*, with values customised for 4H-SiC. This model implements concentration dependent mobility, as formulated in Eq. 4.4.1, and results in a mobility for low electric fields dependent on doping concentration.

The values needed for the low-field mobility model (Eq. 4.4.1) are for electrons set to $\mu_{min,n} = 40$, $\mu_{max,n} = 950$, $N_{ref,n} = 2 \cdot 10^{17}$, and $\alpha_n = 0.76$ [19], while the corresponding vales for holes are $\mu_{min,p} = 0$, $\mu_{max,p} = 114$, $N_{ref,p} = 2.3 \cdot 10^{18}$, $\alpha_p = 0.69$ [20]. No temperature dependence is included, as the temperature in the simulation is kept at a constant 300 K.

Charge carrier mobility is known to be reduced at higher electric fields, and given that SiC Schottky diodes are able to operate under relatively high potentials, the parallel electric field-dependent mobility [13] model was also included with *fldmob* in the **models** statement. This model implements Eqs. 4.4.3 and 4.4.4, which modifies the low-field mobility using a saturation velocity for electrons and holes. These mobility models are able to include temperature dependencies with the inclusion of more variables. Since the simulations were only performed for $T = 300$ K, this was not necessary.

The field dependent mobility model for electrons (Eq. 4.4.3) and holes (Eq. 4.4.4) makes use of velocity saturation, whose values set to $v_{s,n} = 2.2 \cdot 10^7$ cm/s, and $v_{s,p} = 1.3 \cdot 10^7$ cm/s, respectively [4], whereas the β values are kept at their default values [18], namely $\beta_n = 1$ and $\beta_p = 2$.

4.4.2 Carrier Recombination

The recombination of charge carriers can occur through different mechanisms. Shockley-Read-Hall (SRH) recombination is implemented by adding *srh* and is described in Eq. 2.1.17. This model is mainly dependent on deep level traps and charge carrier lifetimes.

Auger recombination is another possibility for charge carrier recombination, whereby an electron recombines and gives its excess energy to another electron in the conduction band, which will then gradually lose its excess energy to its environment. Auger recombination is modelled using the equation [13]

$$R_{Auger} = C_n(pn^2 - nn_i^2) + C_p(np^2 - pn_i^2), \tag{4.4.5}$$

where C_n and C_p are the Auger coefficients for electrons and holes, respectively. It is implemented in the simulation through adding *auger* to the **models** statement. The Auger coefficients used for both electrons and for holes were not changed from their default Si values in Atlas, although these values for 4H-SiC have been reported to be about twice as large than for Si [21]. Additionally, these coefficients are also, temperature [21] and doping concentration [22] dependent.

When implementing traps discovered using DLTS, most parameters could be calculated from those measurements. These being the energy level of the trap, the trap concentration, and electron capture cross section. The degeneracy factor was set to 1, and the capture cross section relating to holes was for simplicity set to the same as that estimated for electrons. One further point to add, regarding the estimation of the capture cross section, is that the value extracted using the Arrhenius plot would strictly be valid for infinitely large temperatures, as the value is taken from the y-axis intercept, rather than closer to expected operating temperature ranges [11]. Furthermore, as an extrapolation is needed to find this intercept, the value is also highly sensitive to errors.

4.4.3 Band Gap Narrowing

To model the narrowing of band gaps seen at higher doping concentrations, the Lindefelt band gap narrowing model [23] was used, and implemented through *bgn.lind*. For an n-doped material the equation for the energy shift in the conduction and valence are respectively

$$\Delta E_C = A_{nc}\left(\frac{N_D^+}{N_D}\right)^{1/3} + B_{nc}\left(\frac{N_D^+}{N_D}\right)^{1/2}, \quad 4.4.6$$

and

$$\Delta E_C = A_{nv}\left(\frac{N_D^+}{N_D}\right)^{1/4} + B_{nv}\left(\frac{N_D^+}{N_D}\right)^{1/2}, \quad 4.4.7$$

where N_D^+ is the ionised donor concentration, while A_{nc}, B_{nc}, A_{nv}, and B_{nv} are material dependent coefficients. The values for n-doped 4H-SiC are given in [23], which are used by default for 4H-SiC simulations in Atlas [13]. This results in a total narrowing in the band gap of

$$\Delta E_G = \Delta E_C + \Delta E_V. \quad 4.4.8$$

4.4.4 Contacts

In the single electrode simulations the top electrode covered the entire top surface of the simulated wafer, giving the device a 1D structure. The back contact similarly covered the underside. Although the top electrodes have a thickness of about 150 nm, they were simulated without physical dimensions in the y-direction, as the area of interest was the semiconductor. The material of the top electrodes was nickel, with properties kept at their default values, except for the **contact** statement. To implement the Schottky contact between the electrode and semiconductor, the **contact** statement includes the *workfunction* value of 5.01 [24], *surf.rec* to enable surface recombination, *barrier* to enable barrier lowering, and the relative effective mass in tunnelling mode for both electrons and holes are set to 0.3 here as well as in the material statement. The back contact was assumed in the simulations as an ideal ohmic contact.

4.4.5 Single Event Upset

The **singleeventupset** statement allows one to simulate charge generation along a track by specifying its entry and exit points, the charge density, how the charge generation is spread radially about the track, and the charge generation over time. The spatial spread of the free charge around the track is expressed by

$$R_b(r) = e^{-\frac{r}{radius}}, \quad 4.4.9$$

where r is distance from the centre of the track and $radius = 1$ µm relates to how spread out the released charges are. One consequence of this radial charge distribution is an additional charge contribution in either end of the track. The amount of total generated charge exceeds the charge expected from purely the given charge per micron and the length of the charge. For the applied parameters, this contribution happens to be approximately 130 q on either end of the track, given that this area is included in the simulations, i.e. not outside of the simulated device.

The rate at which EHPs are released over time is defined by

$$T_b(t) = \frac{2e^{-\left(\frac{t-T_0}{T_C}\right)^2}}{T_C\sqrt{\pi}\,\mathrm{erfc}\left(-\frac{T_0}{T_C}\right)}, \quad 4.4.10$$

where t is time, $T_C = 1$ fs relates to how spread out the released charges are in time, and $T_0 = 5$ fs is the entry time of the track, or rather its temporal centre.

Chapter 5

Results and Discussion

5.1 Measurements

5.1.1 I-V

Plots of the I-V for the four measured diodes, at voltages between -1 and 1 V, can be seen in Fig. 5.1, including their fit to the diode equation (Eq. 3.1.1). Measurements beyond a reverse bias of 1 V are not included. The available measurement setup did not allow for voltages above 10 V, which would not be large enough to cause a measurable leakage current. The accompanying fitting parameters are the ideality factor and reverse bias saturation current. In the first graph with the measurement data from diode *A1*, all values below approximately 0.6 V are in the range 0.1-1 pA, while the current for voltages above this value the plot shows a linear tendency on the logarithmic scale, indicating an exponential relationship between current and applied voltage in the forward direction. In the graph relating to the diode labelled *B2*, this linear tendency starts earlier at approximately 0.3 V, although for this sample the linearity later falls off beyond 0.6 V, meaning the current no longer grows exponentially beyond this point. Diode *C3* is quite similar to *A1*, showing an exponential growth in current after approximately 0.6 V. Lastly, the current in diode *D4* increases exponentially at an applied voltage above 0.7 V. The measurement accuracy of the instrument used on the lowest range is 0.4 pA, which can be seen from all plots in Fig. 5.1. The measured current fluctuated between 0.1 pA and somewhere below 1 pA in the entire range where the actual current was too small to be measured. This indicates a high quality of both the diodes and the experimental setup, since the minimum measured current is defined by the sensitivity of the picoammeter rather than the leakage current of the diodes, or the parasitic shunt resistance of the setup.

The graphs of the measurements are fitted to the Shockley diode equation (Eq. 3.1.1),

through which the ideality factor and an estimated reverse saturation current is found, and the accompanying statistical errors. The data used in the fitting is limited to the data points with currents between 1 pA and 10 nA, in order to exclude data in the range of the measurement limit, and to not use points above which the diode has linear characteristics on the log scale, as the diode equation is not valid beyond that point. Diode *A1* shows an ideality factor of $\eta = 1.25 \pm 0.01$ and a reverse saturation current of $I_0 = (1.3 \pm 0.1) \cdot 10^{-22}$ A. *B2* has a comparable ideality factor of $\eta = 1.19 \pm 0.03$, but its reverse saturation current is much higher at $I_0 = (3 \pm 1) \cdot 10^{-17}$ A, indicating that this diode is not of great quality. The values found for diode *C3* are quite similar to those of *A1*, with an ideality factor of $\eta = 1.21 \pm 0.02$ and a reverse saturation current of $I_0 = (5 \pm 2) \cdot 10^{-22}$ A. The diode showing both the lowest ideality factor and reverse saturation current is *D4*, with an ideality factor of $\eta = 1.03 \pm 0.01$ and a reverse saturation current of $I_0 = (1.6 \pm 0.1) \cdot 10^{-25}$ A. In order to obtain measurements able to discern the reverse saturation current, possible options could be either increased temperature or much higher reverse biases.

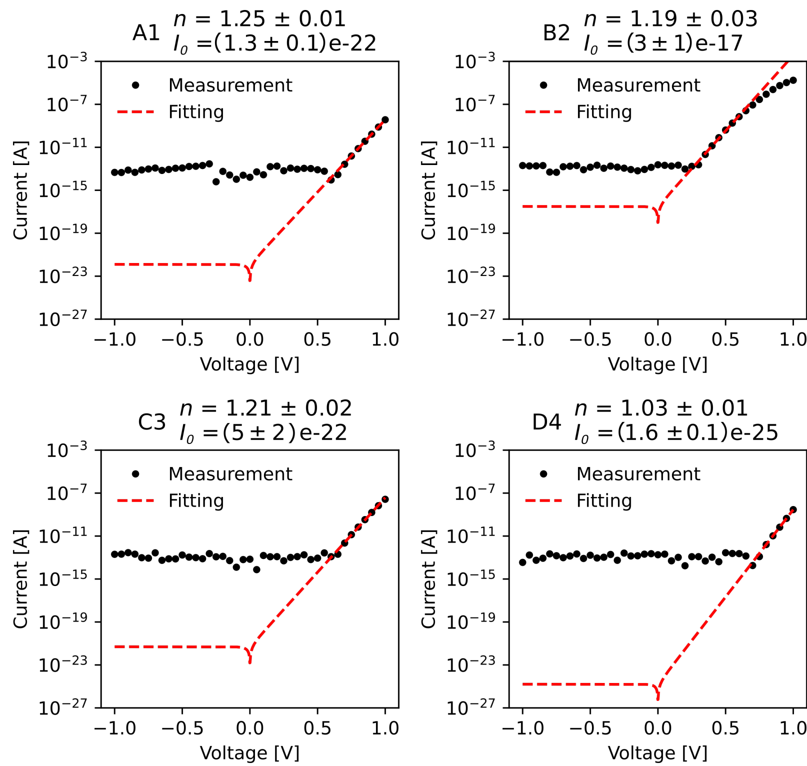

Figure 5.1: Current-voltage measurements of four Schottky diodes from the same wafer (circles) and the fitted Shockley diode equation (dashed curve). Ideality factors, n, and saturation currents, I_0, are found by curve fitting, using the current values between 1 pA and 10 nA. The statistical error of the parameters resulting from the curve fitting is also included.

5.1.2 C-V

The measured capacitance as a function of voltage in the range from 0 to -10 V can be seen in Fig. 5.2a, and as the inverse of the square capacitance in Fig. 5.2b. This

voltage range was limited by the available capacitance meter, meaning voltages high enough to deplete the epitaxial layer or cause breakdown were not available. The measured capacitance value of $5.59 \cdot 10^{-11}$ F at 0 V corresponds to a depletion region of 1.2 ± 0.1 µm from Eq. 3.2.1, given a Schottky diode area of 0.0079 ± 0.0008 cm^2 and SiC relative permittivity of 9.7. While the capacitance value of $2.06 \cdot 10^{-11}$ F recorded at -10 V corresponds to a depletion region of 3.3 ± 0.3 µm. The $1/C^2$-plot reveals a close to linear dependence on voltage, which indicates a fairly uniform doping depth distribution.

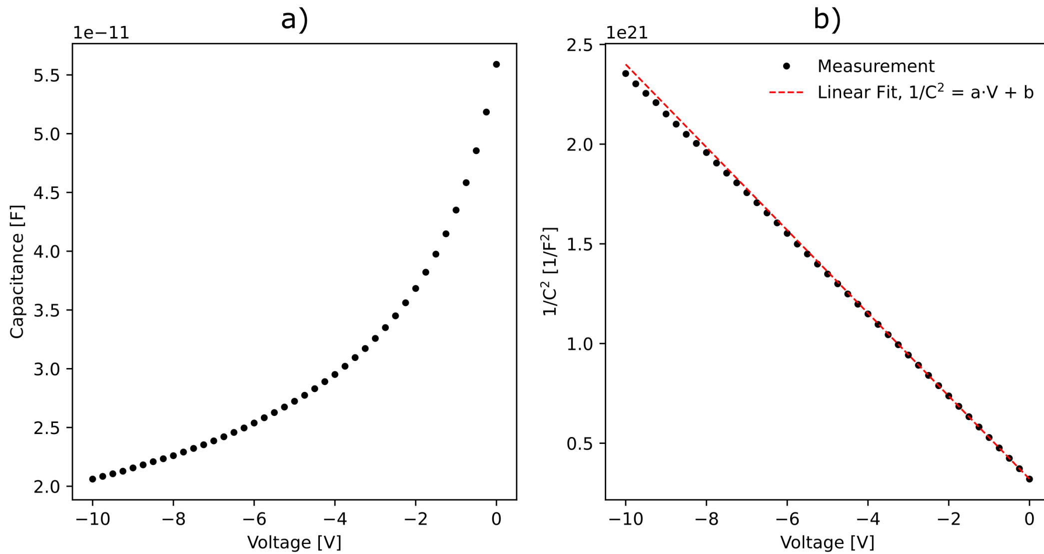

Figure 5.2: a) The capacitance of the simulated Schottky diode plotted as a function of voltage, on a range from 0 to -10 V. b) Shows the inverse square of the capacitance over the same voltage range. Linear regression was performed using the least square error method, giving a slope of $a = -(2.080 \pm 0.002) \cdot 10^{20} \frac{1}{VC^2}$, and an intercept of $b = (3.204 \pm 0.003) \cdot 10^{20} \frac{1}{C^2}$. Although the data in b) is quite linear, it can be seen to deviate slightly from the straight dashed red line depicting the linear regression model.

The linear regression with respect to Eq. 3.2.2 of the $1/C^2$ values seen in this plot was used to calculate a built-in voltage of $V_0 = 1.57 \pm 0.01$ V using Eq. 3.2.5 and a doping concentration of $N_d = (1.1 \pm 0.2) \cdot 10^{15}$ cm^{-3} using Eq. 3.2.6. The uncertainty of the doping concentration is dominated by the 10% error in the diode area. The area is squared in the equation for doping concentration (Eq. 3.2.6) resulting in an uncertainty of 20% from the estimated error in diode radius alone. The statistical errors from the linear regression procedure are much smaller, meaning the relative error in the built-in voltage is smaller. In Fig. 5.2b, the measured capacitance and the linear approximation do not follow each other exactly, they deviate at higher reverse voltages. In order to get a better idea as to how much this deviation is a trend or not, one would want to look at the capacitance over a larger voltage range. A larger voltage range was unfortunately not possible on the available measurement setup.

To have a closer look at the depth distribution, the doping concentration is plotted as a function of the width of the depletion region in Fig. 5.3. The capacitance is used to calculate the depletion region depth using Eq. 3.2.1. The doping concentration is calculated from the gradient of the inverse square of the capacitance (Eq. 3.2.4) after having smoothed the near-linear curve using a Savitzky-Golay filter with subsets of 13 points and polynomial order of 2. The doping concentration is larger further into the epitaxial layer, over the available depletion region window. It shows that the doping concentration in epitaxial layer varies between 1.12 and $1.21 \cdot 10^{15}$ cm^{-3}. Although not strictly linear, there is a clear positive correlation between doping concentration and depletion region. Combined with the uncertainty from the diode area, the doping concentration is on the range $(0.9\text{-}1.4) \cdot 10^{15}$ cm^{-3}.

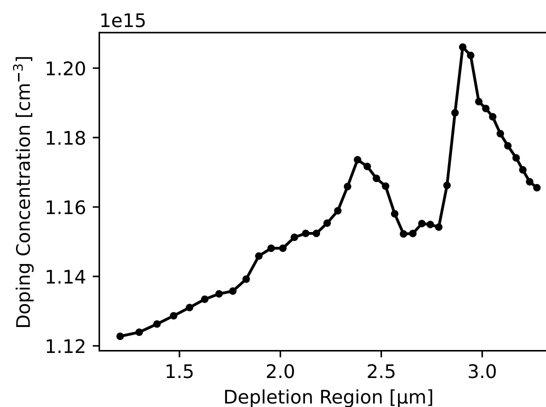

Figure 5.3: The doping concentration of the epitaxial layer as a function of the width of the depletion region.

5.1.3 DLTS

The raw DLTS data, on the temperature range from 83 to 350 K, can be seen in Fig. 5.4. Using this, the energy level, electron capture cross section, and concentration of the two different traps responsible for the peaks around 90 K and 300 K can be calculated.

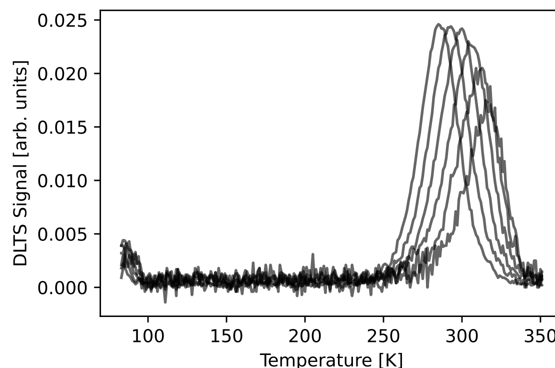

Figure 5.4: A plot of the raw data from the DLTS measurements performed on the temperature range from 83 to 350 K.

It is evident from the data presented in Fig. 5.4 that there is significant noise in the measurements, so to estimate the true height and centre of each peak, they were fitted to Gaussian distributions. Their entire shape does not exactly fit a Gaussian, so the fitting was instead done only using a limited number of points in the vicinity of the top. For the peaks at around room temperature, five points to either side of the top were used, while for the less discernible peaks at and around 90 K, ten points to either side were chosen, with the obvious exception of the cases where there were less than ten available points to the left of the peak, due to the spectrum starting at 83 K.

The temperature found for these peaks were then used to plot Eq. 3.3.3 as a function of inverse temperature, $1/T$, resulting in what is called an Arrhenius plot. The values of e_n for the respective peaks are taken from Table 3.1, and the temperature in the equation must be the temperature at the centre of these peaks. After confirming that this plot showed a linear tendency, the data were fitted using linear regression from which the slope and intercept, with accompanying statistical uncertainties, can be extracted. This linear fit would then look like

$$y = a \cdot x + b, \tag{5.1.1}$$

where

$$y = \ln\left(\frac{e_n}{T^2}\right),\ a = -\frac{\Delta E_t}{k},\ x = \frac{1}{T},\ \text{and}\ b = \ln\left(\sigma_n K_n\right). \tag{5.1.2}$$

The slope, a, can be used to find the energy level of the trap responsible for the plotted peak

$$\Delta E_t = -a \cdot k, \tag{5.1.3}$$

and the intercept, b, could be used to estimate the capture cross section

$$\sigma_n = \frac{e^b}{K_n}. \tag{5.1.4}$$

An issue with using the intercept to estimate the capture cross section of the trap is that this would be the value at $T \to \infty$, as the intercept is where $x = 1/T = 0$. Additionally, this value is highly prone to errors [11], and should thus ideally be found using another method. For the Arrhenius plot relating to the peaks around room temperature, all six peaks were utilised. However, for the traps seen at the lower end of the

temperature range, the two peaks with the longest time windows did not fall within the measured temperature range, hence only four points were included.

Lastly, the concentrations for the two types of traps were calculated using Eq. 3.3.9. The value used for N_d was that found from the previous capacitance measurements, the values used for ΔC were found using the values in Table 3.1 in combination with the measured height of the peaks, S_{max}, as well as using the accompanying C_{rb} values measured during the experiment at the temperature corresponding to the respective peaks.

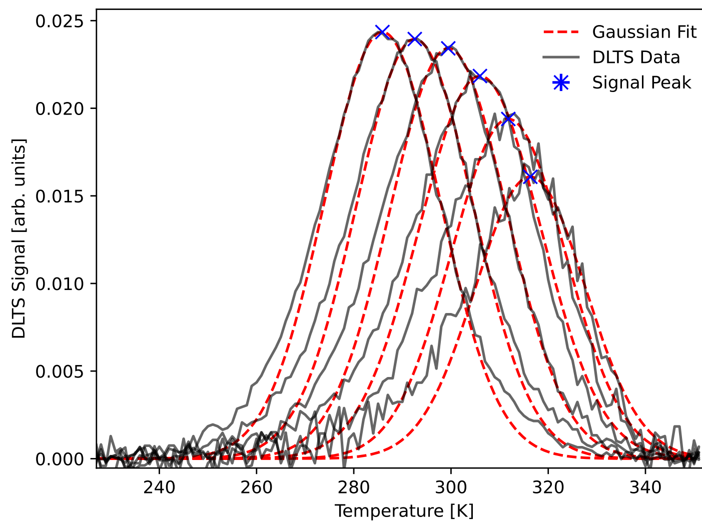

Figure 5.5: A Gaussian distribution is used to estimate the height and centre of the DLTS signal peaks located at around 300 K. The standard deviations for the mean of the Gaussian peaks ranged from 0.005% to 0.03% of the mean value, while the standard deviation for the height of the peaks ranged from 0.04% to 0.2% of their respective heights.

Prior to performing any calculations using the obtained DLTS data, the background noise was estimated by calculating the mean signal value between 100 K and 240 K, and subtracting these six values from each of the six individual graphs in an effort to mitigate systematic errors.

The determination of the real position of the peak in the DLTS signals around room temperature can be seen in Fig. 5.5, where the temperature and height of the peak is plotted, including their standard deviation resulting from the Gaussian fit. One can also see that the peak does not as a whole follow a Gaussian distribution, and so a more apt distribution might exist. The fact that relatively few points were used to estimate the peak is not ideal, but the resulting error is small enough for it to be reasonable, exemplified by the error bars being too small to stand out in on the plot.

The accompanying Arrhenius plot can be seen in Fig. 5.6, where the data points from

the results of the Gaussian fit are used, and a linear fit of these data points is overlaid. The energy level of this deep level trap was determined to be $E_t = 0.69 \pm 0.01$ eV, which corresponds to a type of trap labelled as $Z_{1/2}$, caused by carbon vacancies in the hexagonal and cubic lattice sites in the 4H-SiC crystal structure [25]. Individually, these would be labelled as Z_1 and Z_2, respectively, but can not be distinguished using this standard DLTS technique [25].

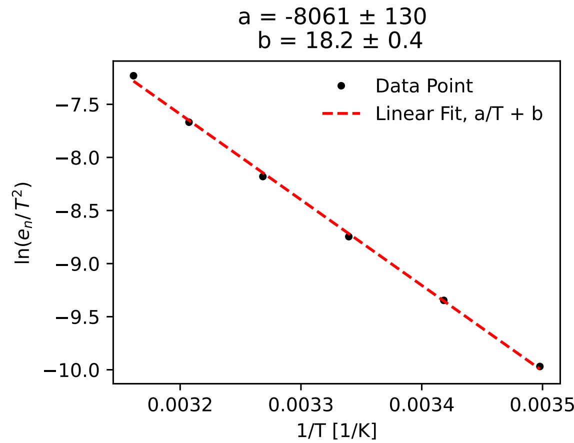

Figure 5.6: The Arrhenius plot created using the peaks from Fig. 5.5 and an accompanying linear fit to the data.

The calculated electron capture cross section was $\sigma_e = (2.3 \pm 1.2) \cdot 10^{-14}$ cm^2. As was mentioned previously this value is calculated from the intercept of the y-axis, which in this case is an extrapolation to $1/T \rightarrow 0$, or $T \rightarrow \infty$, so this is not the ideal method for extracting the capture cross section of the trap, in addition to it yielding a large error. The calculated concentration of the $Z_{1/2}$ trap was $N_t = (2.19 \pm 0.13) \cdot 10^{13}$ cm^{-3}, which for reference is about 50 times lower than the measured doping concentration of the epitaxial layer.

Similarly to the DLTS data for the $Z_{1/2}$ trap, the four DLTS peaks seen at the lower end of the temperature range can be seen in Fig. 5.7, in addition to the positions of the peaks estimated from the Gaussian fit, as well as the Gaussian distribution itself. The error bars for these peaks are more pronounced, with the largest relative error being for the height of lowest of the four peaks, at about 3.5%.

An Arrhenius plot was also constructed from these four data points, which can be seen in Fig. 5.8. The energy level of this deep level trap was calculated to be $E_t = 0.18 \pm 0.02$ eV. From this, it was determined that the trap responsible for these peaks is likely substitutional Ti in the cubic Si lattice site [25] [26]. The electron capture cross section for the Ti traps was from the fitting found to be $\sigma_e = (4 \pm 107) \cdot 10^{-14}$ cm^2. Notably, the resulting error from the extrapolation is more than 26 times larger than the value

itself, revealing the large inaccuracy of this measurement. And again, this would be valid for the theoretical temperature limit $T \to \infty$.

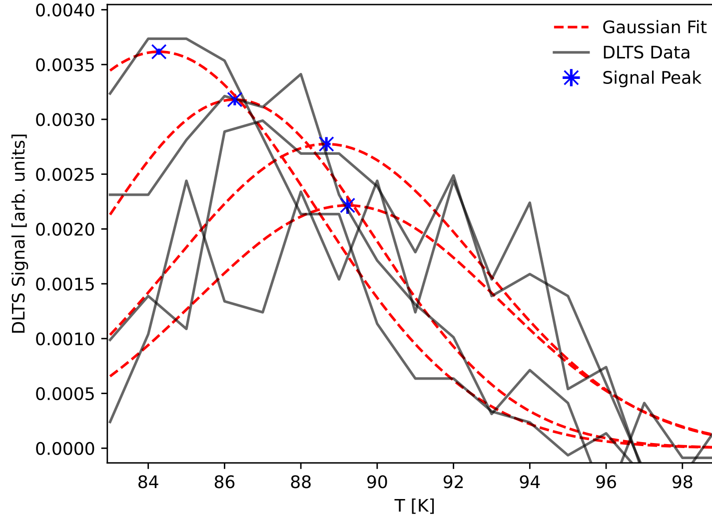

Figure 5.7: A Gaussian distribution is used to estimate the height and centre of the DLTS signal peaks located at around 85 K. The standard deviations for the mean of the four Gaussian peaks were all between 0.1 and 0.2 % of the mean value, while the standard deviation for the height of the peaks ranged from 0.8 % up to 3.5 %.

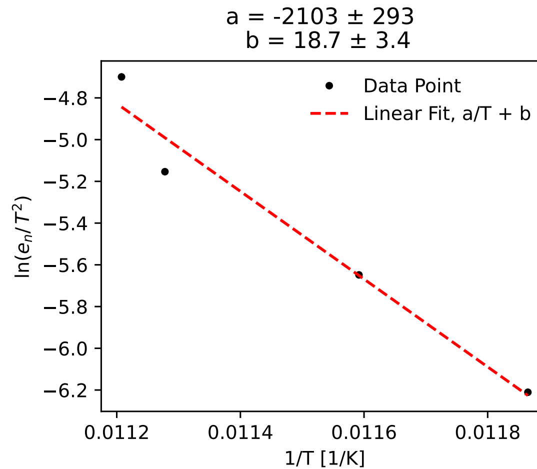

Figure 5.8: The Arrhenius plot created using the peaks from Fig. 5.7 and an accompanying linear fit to the data.

The calculated concentration of the Ti trap is $N_t = (3.2 \pm 0.3) \cdot 10^{12}$ cm^{-3}, which in comparison is about 350 times lower than the measured doping concentration of the epitaxial layer. There are two main reasons why the resulting errors are larger for the data relating to the Ti traps than the $Z_{1/2}$ trap. Firstly, the fact that the absolute value of the signal is lower due to the lower trap concentration, making it more prone to fluctuation. And secondly the absence of the two peaks with the longest time step

resulting in two fewer points from which to fit the linear model. These two missing peaks also happen to be the ones which would have been most accurate, due to the longer time windows used to build those graphs.

5.2 Simulation

5.2.1 I-V

The simulated current for voltages between 1 and −1 V can be seen in Fig. 5.9, where it is compared to the measured currents from diode *D4* (Fig. 5.1). In order to properly scale the simulated currents to those measured from the 1 mm diameter diodes, it has been multiplied with a factor of 785.4. This is because the simulated diode has a width of 1 mm to match the electrode diameter, and the length of the dimension pointing into the plane (the z-axis) is by default set to 1 µm.

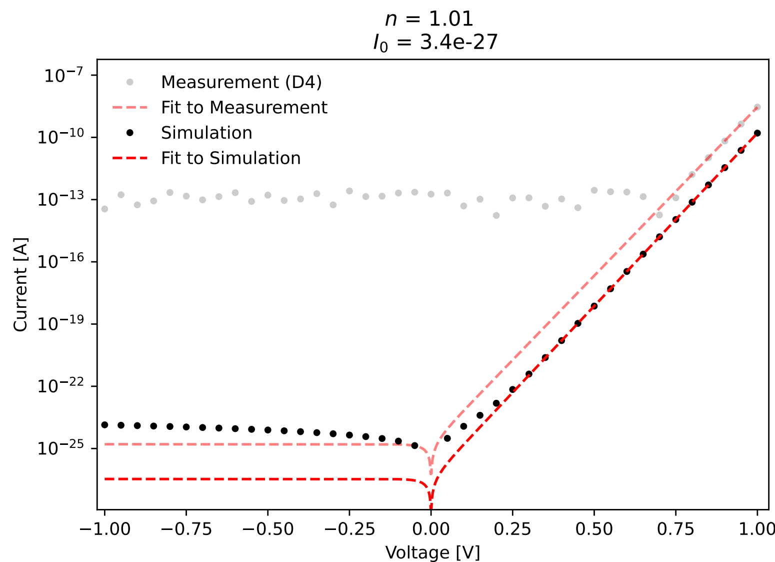

Figure 5.9: A comparison between I-V characteristics of the experimental data from diode *D4* and the simulated 1D Schottky diode. The curve fitting of the Schottky diode equation is included for both. The fit of the simulated data gives an ideality factor of $\eta = 1.01$, and a saturation current of $I_0 = 3.4 \cdot 10^{-27}$ A.

There is no obvious issue with a measurement limit for simulated data, so the difference between the measured and simulated currents is large below 0.7 V. Diode *D4* was chosen for the comparison since it most resembled the simulated data, with it having the lowest reverse saturation current and ideality factor. Similar to the analysis of the experimental I-V data, the simulated data were also fitted with the Shockley diode equation (Eq. 3.1.1) using data points with currents between 10^{-18} and 10^{-8} A. The

fit of both diode *D4* and the simulated data are included in Fig. 5.9. The fit of the simulated data show a reverse saturation current of $I_0 = 3.4 \cdot 10^{-27}$ and ideality factor of $\eta = 1.01$, versus the $I_0 = (1.6 \pm 0.1) \cdot 10^{-25}$ and $\eta = 1.03 \pm 0.01$ estimated for diode *D*4.

The reverse saturation current in the simulated device does not follow the current predicted by the Shockley diode equation even at very low reverse biases, increasing in magnitude rather than staying constant as the Shockley diode equation would suggest. This is likely due to the simulations taking into account more physical models, giving a more accurate prediction for very low currents in a Schottky diode.

Although the currents in the physical component could not be measured at large reverse biases due to the available equipment, this could be estimated through simulations. In Fig. 5.10 the simulated current is plotted in the range between 0 and 1650 V, using four different combinations of implemented models. All four combinations include the models used in other simulations, *analytic*, *fldmob*, *srh*, *auger*, and *bgn.lind*. However, in order to be able to simulate breakdown characteristics which occur at higher reverse voltages, simulations with impact ionisation and/or band-to-band tunnelling (BBT) are also included.

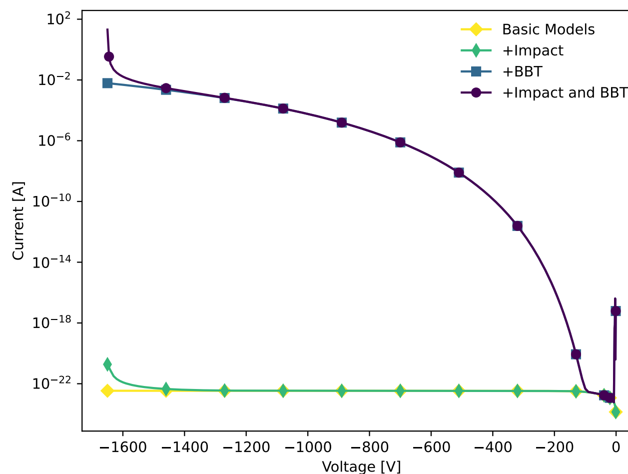

Figure 5.10: Reverse bias current for the simulated 1D device, using four different combinations of models. Using the models implemented for other simulations as a reference, the effect of adding band-to-band tunneling and impact ionisation models are seen through the four different I-V characteristics.

Avalanche breakdown can be seen to occur at reverse voltages above 1600 V, while band-to-band tunnelling has a significant impact on the leakage current at voltages above 100 V. This is not compatible with known facts from practical applications of SiC diodes operating at high reverse bias voltages. This indicates that the BBT model can not describe the diodes adequately or that the parameters chosen from [16] are not applicable in this case. Besides, for voltages below about 10 V, the inclusion of the

band-to-band tunnelling model appears to cause quite significant instabilities. The BBT model was not included in further simulations.

5.2.2 C-V

The simulated capacitance for voltages between 0 and -10 V compared with the measured capacitance can be seen in Fig. 5.11a, while the inverse of the square capacitance of both is plotted in Fig. 5.11b. The linear regression procedure is again performed, highlighting the fact that there is no noticeable drift from linearity in the simulated device over this voltage range. Using the simulated data to calculate built-in voltage using Eq. 3.2.5 and donor concentration using Eq. 3.2.6 to further verify the validity of the model gave $V_0 = 1.50$ V and $N_d = 1.14 \cdot 10^{15}$ cm^{-3}, respectively. Although there is a 70 mV difference between the built-in voltage from the simulated and the measured data, the comparison shows that there is clear consistency in capacitance between the simulation and the device it is meant to replicate. The simulations naturally also shows uniformity in the doping concentration, in contrast with the measurements.

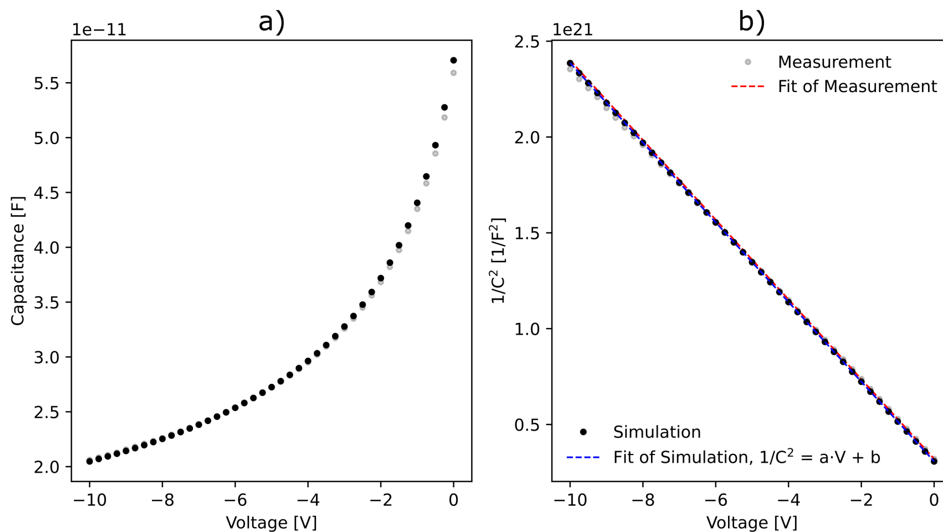

Figure 5.11: a) A comparison between measured and simulated Schottky diode capacitance plotted as a function of voltage, on a range from 0 to -10 V. b) The inverse square capacitance is plotted on over the same range. The linear regression procedure gave a slope for the simulated data of $a = -2.08 \cdot 10^{20}\ \frac{1}{VC^2}$, and an intercept of $b = 3.07 \cdot 10^{20}\ \frac{1}{C^2}$. The simulated data does not deviate from the dashed red line, which depicts the linear regression model of the simulated data.

Despite not being able to measure the capacitance of the device over a large voltage range, this could easily be simulated. Fig. 5.12a shows the capacitance of the simulated diode between 0 and -500 V. Whereas in Fig. 5.12b, the inverse square of the simulated capacitance is plotted. The linearity of the $1/C^2$ data clearly ends at around -100 V, after which the $1/C^2$ values quite abruptly saturate, indicating that full depletion

of the epitaxial layer is reached. At this point entire epitaxial layer is depleted, and further increase in voltage prior to breakdown will lead to depletion of the more highly doped buffer layer underneath. Due to the higher doping concentration, the width of the depletion region now changes much more slowly, making it appear constant as voltage is increased further. This observation matches with the value calculated by solving Eq. 2.2.6 for V with the width set to the thickness of the epitaxial layer, 10 µm, as well as the built-in voltage and doping concentration found from the capacitance measurements, resulting in a prediction of complete depletion at just over 104 V.

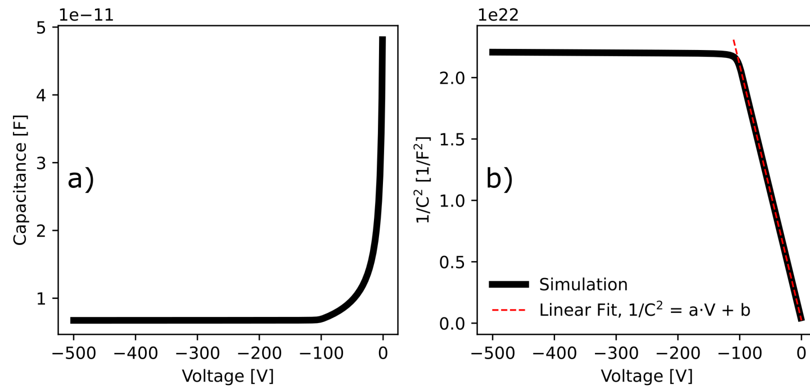

Figure 5.12: a) The simulated capacitance plotted as a function of voltage, on a range from 0 to −500 V. b) Inverse square of the capacitance as a function of voltage. In order to visualise the linearity seen in b), a linear regression over the first 50 V can be seen by the red dotted line. At just about −100 V, the capacitance clearly deviates from the linear tendency due to saturation of the epitaxial layer.

5.2.3 Transient Simulations

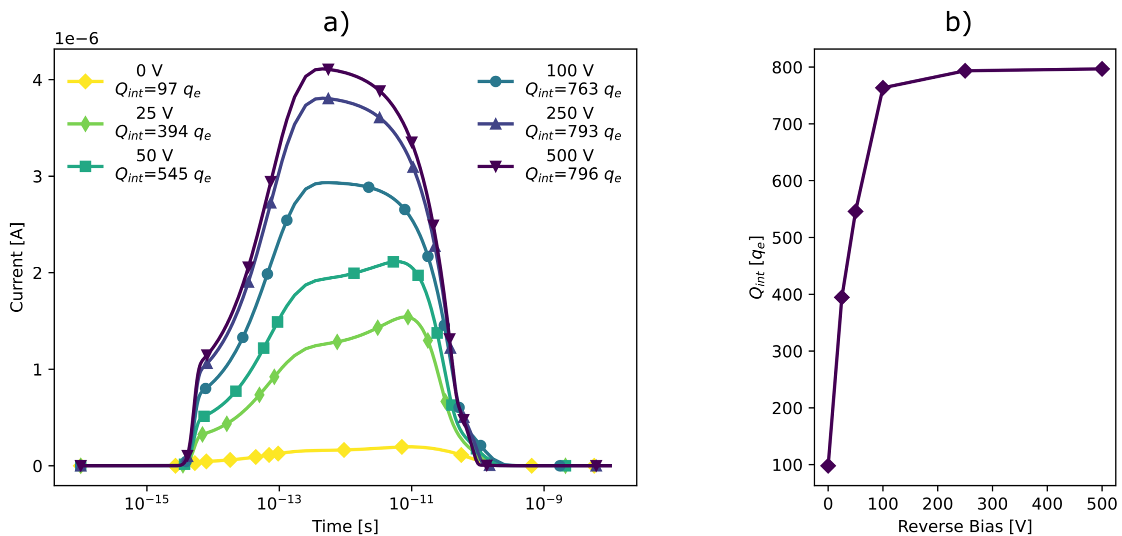

Figure 5.13: a) Transient simulations where the current is plotted over time with applied voltages between 0 and 500 V, with the simulated radiation track entering at $t = 5 \cdot 10^{15}$ s. The current collection happens faster when the applied voltage is higher. b) A plot of the charge collection, Q_{int}, as a function reverse bias voltage. The CCE can be seen to increase with applied voltage, and at 100 V the CCE is almost maximised.

The charge collection from the incident radiation, which is simulated as free charge carriers released along a track going vertically through the semiconductor device, releasing 80 q/µm along its path, is simulated under different conditions. Simulated transient currents for applied bias voltages of 0, 25, 50, 100, 250, and 500 V are shown in Fig. 5.13a. The accompanying collected charge calculated through integration of this current can be seen as a function of voltage in Fig. 5.13b.

In agreement with the previous capacitance simulations, the charge collection is almost saturated at an applied bias of 100 V, which matches the expected full depletion voltage of 104 V. This shows consistency between the capacitance simulations, the charge collection simulations and the theory of the depletion region combined with the physical measurements on the device on which the simulations are based.

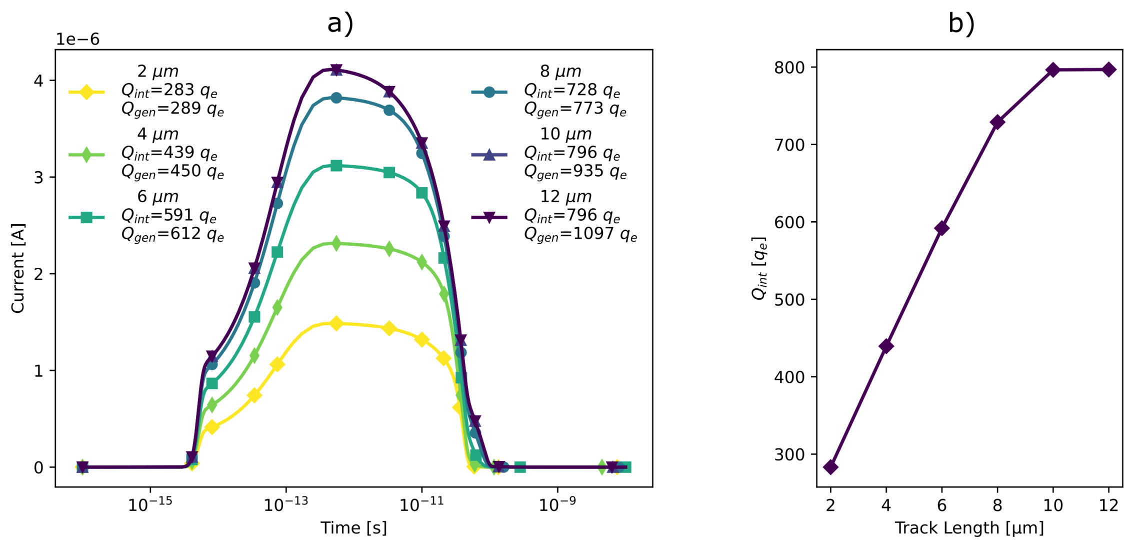

Figure 5.14: a) Transient simulations where the current is plotted over time with an applied voltage of 500 V, with the simulated radiation track entering at $t = 5 \cdot 10^{15}$ s. The penetration depth of the 80 q/µm radiation track is varied between 2 and 12 um, with 2 µm intervals. For each of the six tracks, one can see the integrated charge, Q_{int}, calculated from the transient current, as well as the amount of total generated charge, Q_{gen}, stated in the output files. b) An accompanying plot of the integrated charge as a function of track length.

The results from simulating varying depths of penetration for the radiation track can be seen in Fig. 5.14a, where the transient current is plotted for track lengths of 2, 4, 6, 8, 10, and 12 µm, all entering from the top of the device. The collected charge increases linearly with the length of the track in Fig. 5.14b, up until the penetration depth is about the same as the epitaxial film thickness. The simulations are all performed at an applied bias of −500 V and with the same set of parameters as in the simulations in Fig. 5.13a. The integrated charge is shown, in addition to the amount of total generated charge in the simulation. This value differs from the value expected from the charge density of 80 q/µm by about 130 q for all these simulation, as the density tapers

off gradually beyond the specified entry and exit points, in the same way it is also horizontally distributed around the track as stated in Eq. 4.4.9. Comparing the generated charge, Q_{gen}, and the collected charge, Q_{int}, one can observe that the CCE is close to 100% for all penetration depths that release its charges within the thickness of the epitaxial film. The simulations for track lengths of 10 µm, where a significant portion of the charge is released in the buffer layer, and 12 µm result in the same amount if Q_{int}. Concluding that charges released in the buffer layer and in the substrate are quickly recombined and thus have no noticeable impact, in agreement with expectations.

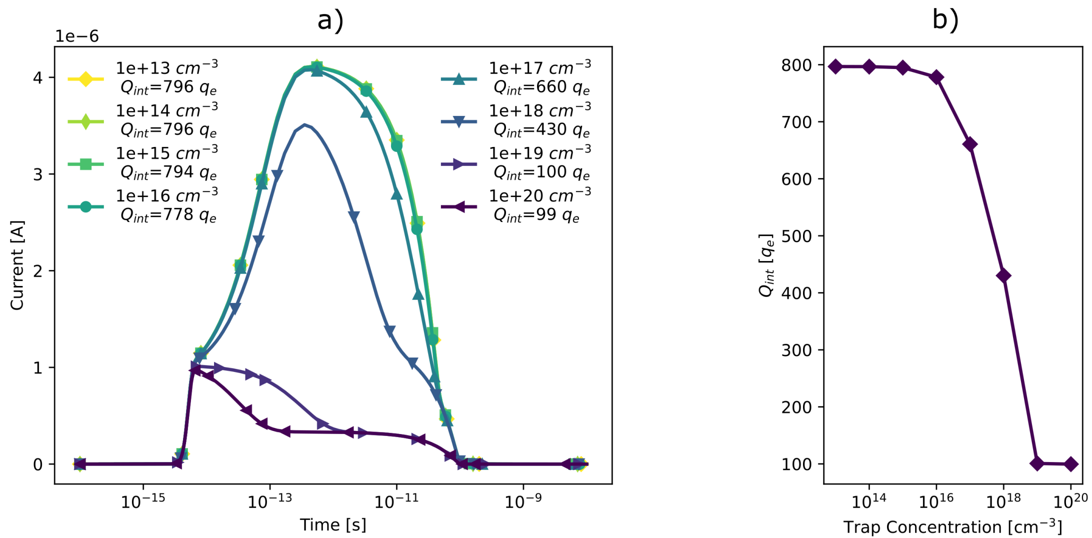

Figure 5.15: a) Plots of the current during transient simulations with a simulated radiation track entering at $t = 5 \cdot 10^{15}$ s, for eight different $Z_{1/2}$ deep level trap concentrations between 10^{13} and 10^{20} cm-3. b) A plot of the integrated charge as a function of trap concentration, to help visualise the impact of trap concentration on CCE. The value of the integrated charge in units of elementary charges is labelled as Q_{int} for each of the eight concentrations. The reverse bias voltage was kept constant at 500 V.

In Fig. 5.15a the transient currents for different concentrations of $Z_{1/2}$ deep level traps can be seen, while their effect on the CCE is summarised in Fig. 5.15b. The value of the concentrations begin at 10^{13} cm^{-3}, around the concentration measured in the physical device from DLTS, and ends at 10^{20} cm^{-3}, beyond what would be considered realistic values. From the eight graphs, and the resulting integrated charge for each of them, the traps do not impact the transient current noticeably before the concentration exceeds 10^{15} cm^{-3}, a concentration close to the doping concentration in the epitaxial layer. The trap concentration does not appear to become detrimental to the CCE until it exceeds 10^{16} cm^{-3}. The main cause of the decrease in current is believed to be the increased recombination rate of EHPs caused at higher trap concentrations, as there will be an increase in the concentration of recombination centres [27].

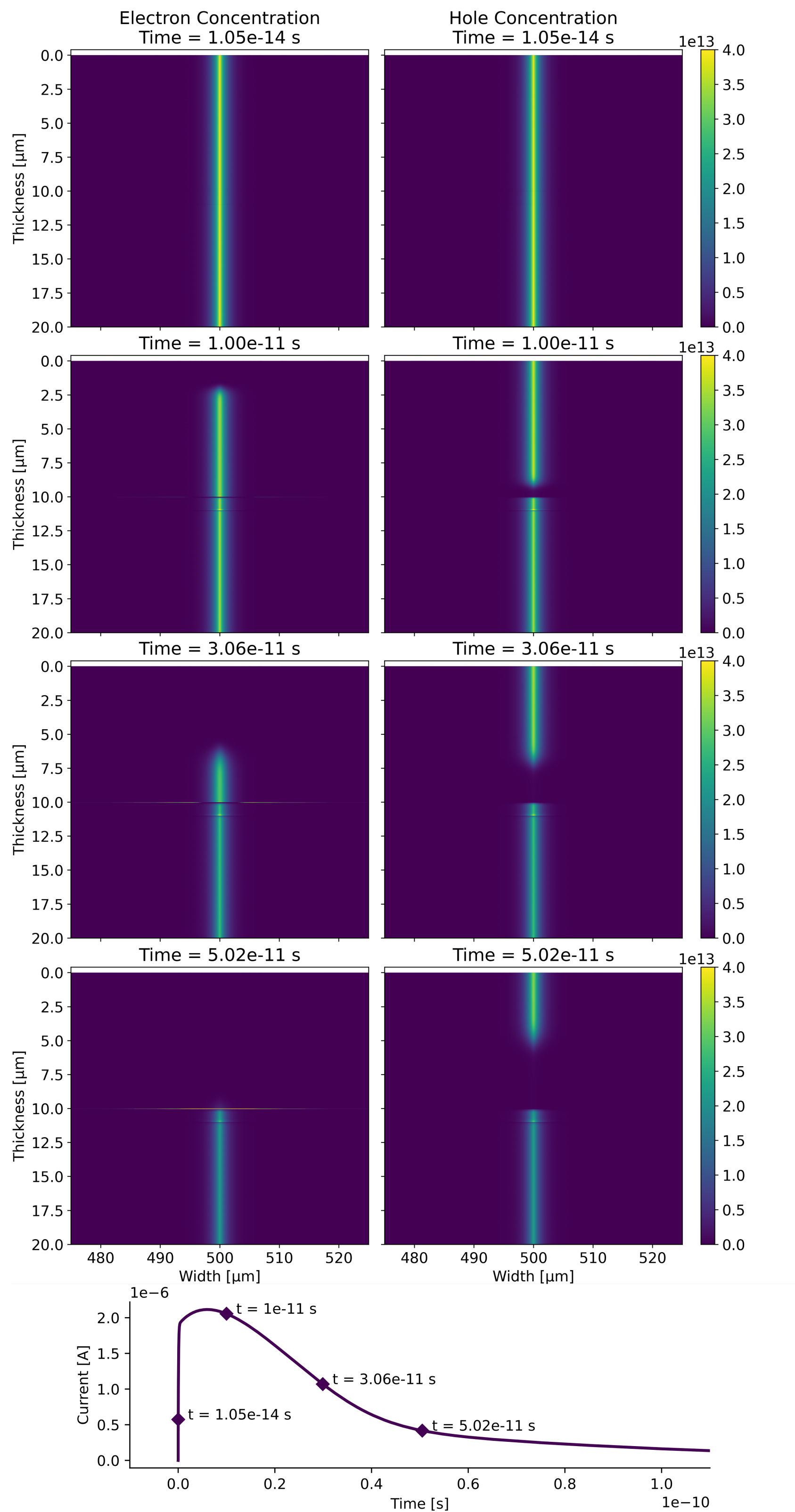

Figure 5.16: The concentration of free electrons and holes in the simulated Schottky diode are plotted side by side at four different points in time, chosen to visualise the movement of the charge carriers following the radiation track. The track penetrates the entire device, and the applied bias voltage is set to 500 V. A limited cross section of the device is shown, focusing on the released carriers in the 10 µm thick epitaxial layer. At the bottom, a plot of the current over the first 0.1 ns is shown, with a marker at each of the four time points used for the above visualisations.

The 2D distribution of electron and hole density at different times in simulations with an applied reverse bias of 500 V, and the radiation track penetrating the entire wafer, can be seen side by side in Fig. 5.16. Four time steps were selected to present a visual perception of how the charge carriers move within the device. The negatively charged free electrons move downwards into the device, while the holes move upwards towards the electrode. This is consistent with the electric field in a Schottky diode pointing towards the electrode, since the depleted ions in an n-type material are positive. Furthermore, the electrons leave the epitaxial layer faster, meaning they will also be measured slightly quicker, which is consistent with their mobility being higher.

5.2.4 Strip Detector Model

The electric field underneath the three 10 μm electrodes in the simulated strip detector with an applied bias of 400 V is shown in Fig. 5.17. The field is largest at the electrode edges, and extends throughout the epitaxial layer. It does not extend into the highly doped buffer layer, which starts at a depth of 10 μm. The electric field does not extend laterally between the electrodes at the very top, but it is more uniform deeper into the epitaxial layer.

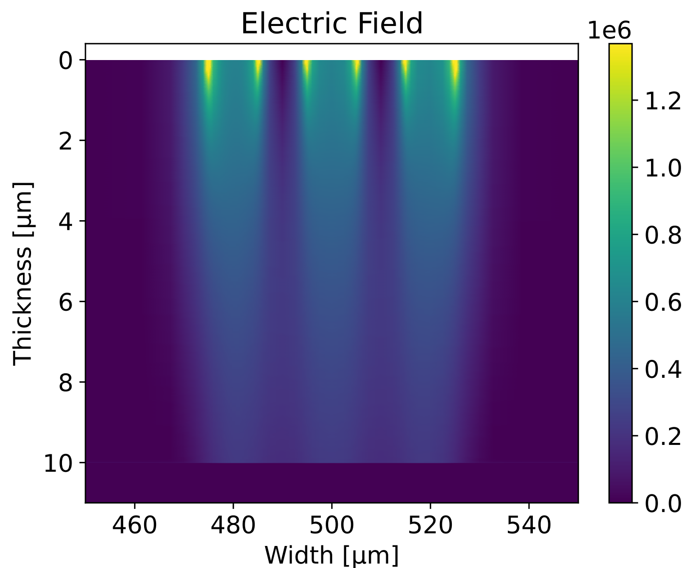

Figure 5.17: The electric field in epitaxial and buffer layer set up by an applied reverse voltage of 400 V, for the design with 10 μm width and spacing for the electrode strips.

Simulations of different designs for a microstrip detector with spacings of 10 μm and 20 μm can be seen in Fig. 5.18, where the total charge collection from the three implemented electrodes is plotted as the position of the vertical track is varied. As expected, the charge collected at an electrode is high when the beam hits at, or in the vicinity of,

that electrode. For the higher voltages, the charge collected from an electrode is seen to be largest at around the edge of the electrodes. This is perhaps not as strange as one might imagine, because this is where the electric fields below electrodes are highest. It is clear that the CCE in the space between the electrodes is highest for the design with the smallest gap, although this can be remedied by applying larger bias voltages. As expected, there is practically no collected charge from the third electrode, which can be seen in the very bottom of the plots.

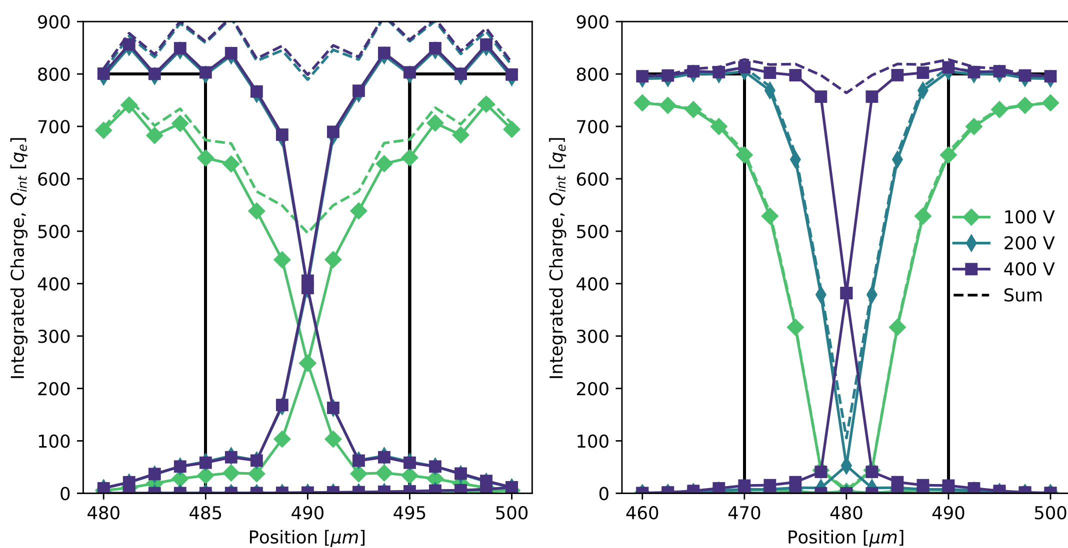

Figure 5.18: Charge collection as a function of the incident position of the vertical track across the microstrip electrodes with a spacing of 10 µm (left) and 20 µm (right). The centre of each plot is the centre between the two left-most electrodes, while the data starts and ends at the centre of the first and second electrode, respectively, meaning that two electrode halves are in view. The boundary of the electrodes is depicted by the black vertical line, while there is a horizontal line at the electrodes, with its height set to the the maximum charge expected from the previous single electrode simulations, 800 q. The charge collected from the three individual electrodes is plotted, and can be seen to have their peak around the centre of their respective electrode. The sum of the contribution from all three electrodes is plotted as dashed lines.

In Fig. 5.19 one can see the simulated charge collection across the three designs with 10, 20, and 30 µm wide electrodes and a 10, 20, and 30 µm wide gaps between them, respectively, all under the applied bias of 400 V. The combination of an applied reverse bias of 400 V and a gap of 30 µm does not lead to complete charge collection in the gap, and no overlap between electrodes. For the 30 µm design to be viable, an even higher applied voltage is needed.

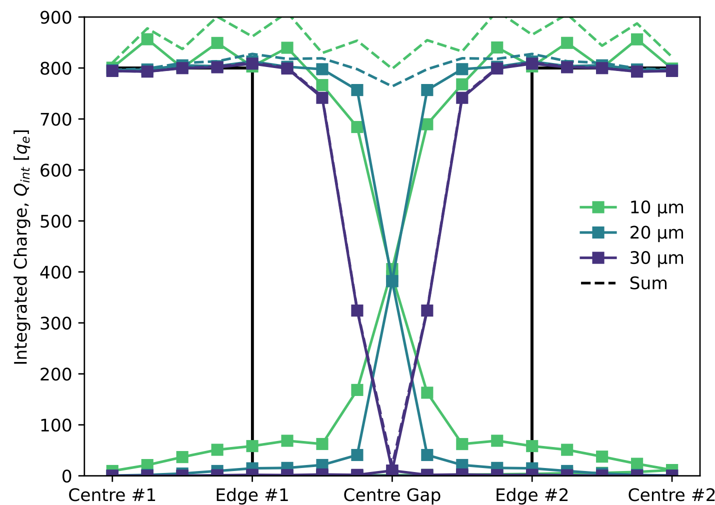

Figure 5.19: In this plot the three different designs, having 10, 20, and 30 µm gaps, respectively, are shown together all with an applied reverse bias of 400 V. Both the design with gaps of 10 and 20 µm show good CCE across the entire gap, while in the centre of one with a 30 µm wide gap, there is practically no charge collection occurring in and around the centre between the two electrodes. Since the dimensions of these three are different, the positions are labelled relative to electrode number one and two, where #1 refers to the first electrode and #2 refers to the second, counting from the left.

The simulated charge collection is the most uniform in the 20 µm design, biased with 400 V. For the 10 µm design, the small gap between electrodes results in increased charge sharing between neighbouring strips. This can be advantageous for reconstructing the impact position of the particle, where one might calculate the weighted average of the charge collected in adjacent electrodes as a function of the x-coordinates of the active strips.

Chapter 6

Summary

In this thesis the electrical characteristics of 4H-SiC Schottky diodes have been studied, through I-V, C-V, and DLTS measurements. These characteristics were then utilised for the implementation and verification of a numerical model for the diodes. The model was then used to simulate the transient current over the diode caused by impacting radiation. It was further expanded to a strip detector design, for the purpose of proposing a feasible radiation detector design.

6.1 Conclusion

The I-V characteristics of four of the sample diodes were measured. By fitting the results to the Shockley diode equation (Eq. 3.1.1), their ideality factors were found to range from $\eta = 1.03$ to $\eta = 1.25$, while the obtained reverse saturation currents ranged between $I_0 = (1.6 \pm 0.1) \cdot 10^{-25}$ and $I_0 = (3.1 \pm 1) \cdot 10^{-17}$ A. The range in values for these parameters indicate variation in the quality of the diodes over the sample.

Measurements of the C-V characteristics were then performed. Linear regression of the analytical expression (Eq. 3.2.2) to the inverse square of the measured capacitance was performed across the voltage range between 0 and -10 V. From this, the doping concentration of the epitaxial layer was determined to be in the range between 0.9 and $1.4 \cdot 10^{15}$ cm^{-3}, increasing further into the epitaxial layer. Both the depth profile and the uncertainty in the electrode area contribute to the uncertainty in doping concentration. Using linear regression, the built-in voltage of the diode was from fitting found to be $V_0 = 1.57 \pm 0.01$ V.

From DLTS, the presence of two types of deep level traps in the semiconductor were detected, the defects responsible for these trap levels were identified through their energy levels of $E_t = 0.69 \pm 0.01$ eV and $E_t = 0.18 \pm 0.02$ eV as carbon vacancies

labelled $Z_{1/2}$ and substitutional Ti defects, with concentrations of $N_t = (2.19 \pm 0.13) \cdot 10^{13}$ cm^{-3} and $N_t = (3.2 \pm 0.3) \cdot 10^{12}$ cm^{-3}, respectively.

The experimentally obtained values were then used as input parameters in the simulations.

The simulated I-V characteristics most resembled the diode with the lowest ideality factor, with it having an ideality factor of $\eta = 1.01$ and a reverse saturation current of $I_0 = 3.6 \cdot 10^{-27}$. Breakdown could be investigated with help of these simulations, and showed avalanche breakdown of the diode at a reverse current of about 1600 V.

Capacitance simulations gave very similar values to the measurements, although the simulation yielded a more linear curve, since the simulated doping profile is completely uniform. Given a 10 µm thick epitaxial layer, the simulated capacitance at high applied voltages predicted the full depletion at just above 100 V through saturation of the capacitance, in agreement with the value of 104 V from the equation for the depletion region (Eq. 2.2.6).

The charge collection from the integration over the transient current caused by the simulated radiation track was recorded under different conditions. One of these were different applied voltages with the radiation track penetrating the entire device. From this it was seen that increasing the reverse bias also increased the amount of collected charge, up to about 100 V where the depletion region extends over the entire epitaxial layer.

Another condition which was tested was varying the penetration depth of the radiation track, with a constant reverse bias of 500 V. This made apparent that the charges released in the epitaxial layer are detected, while charges released in the highly doped buffer layer or substrate are not.

Further, simulations including the $Z_{1/2}$ trap were performed for concentrations up to $N_t = 10^{20}$ cm^{-3}. These simulations showed that concentrations of about 10^{15} - 10^{16} cm^{-3} were needed to impact the charge collection from the simulated radiation. Hence, this type of trap should not impact the behaviour of the Schottky detector, even in larger concentrations.

The charge collection across the strip detectors was then investigated. As expected, even charges released in the gap between neighbouring electrodes can be detected, but to achieve good CCE the voltage must be well above 100 V, which is required for full depletion of the epitaxial layer in the single diode simulations. The combination of a bias voltage of 400 V and 20 µm spacing between electrodes shows the most uniform total charge collection as a function of track position. The design with only 10 µm

spacing between electrodes show a better overlap in charge collection.

6.2 Future Work

Although the leakage current of the diodes could not be measured in this thesis, an effort could be made to reach leakage current large enough for measurements through increased temperature and/or larger reverse biases. If possible, the bias should be increased until reverse breakdown occurs. With a voltage range slightly beyond 100 V, the capacitance could be measured as the depletion region expands over the entire epitaxial layer, which could be used to verify both its thickness and doping uniformity throughout the entire layer.

One aspect which could be important to investigate, that could not be done within this thesis, is to quantify how the electrical properties of the diode are affected by radiation, through irradiation of the sample. Results from this could then be implemented in simulations of the Schottky detector, so that the impact of radiation exposure on the performance of the detector could be assessed for the type of defects caused by radiation exposure. Further simulations could then be performed to obtain a broader picture of the effect of different radiation doses through freely varying the defect concentration.

More combinations of designs and voltages can be investigated, but in order to test these designs in a real setting, and getting a basis for comparison for the simulations, physical detectors of a desirable design should be produced and tested as radiation detectors. Its performance as a radiation detector should then be tested by performing transient measurements to determine its response to impacting ionising particles, using for example electrons, protons, neutrons or gamma radiation.

Bibliography

[1] Mordor Intelligence. *Radiation Detection, Monitoring, and Safety Market | 2022 - 27 | Industry Share, Size, Growth - Mordor Intelligence*. en. Tech. rep. 2021. URL: https://www.mordorintelligence.com/industry-reports/radiation-detection-monitoring-and-safety-market-industry.

[2] Mirion Technologies. *Introduction to Radiation Detectors*. URL: https://www.mirion.com/learning-center/radiation-detector-types/introduction-to-radiation-detectors (visited on 05/02/2022).

[3] Sally Seidel. "Silicon strip and pixel detectors for particle physics experiments". en. In: *Physics Reports*. Silicon strip and pixel detectors for particle physics experiments 828 (Oct. 2019), pp. 1–34. ISSN: 0370-1573. DOI: 10.1016/j.physrep.2019.09.003.

[4] "Appendix C: Major Physical Properties of Common SiC Polytypes". en. In: *Fundamentals of Silicon Carbide Technology*. John Wiley & Sons, Ltd, 2014, pp. 521–524. ISBN: 978-1-118-31353-4.

[5] Charles Kittel. *Introduction to Solid State Physics*. English. 8th Edition. Hoboken, NJ: Wiley, Nov. 2004. ISBN: 978-0-471-41526-8.

[6] Simon M. Sze and Kwok K. Ng. *Physics of Semiconductor Devices*. English. 3rd edition. Hoboken, N.J: Wiley-Interscience, Oct. 2006. ISBN: 978-0-471-14323-9.

[7] Ben Streetman and Sanjay Banerjee. *Solid State Electronic Devices Global Ed*. English. 7th edition. Boston Munich: Pearson, Jan. 2015. ISBN: 978-1-292-06055-2.

[8] W. Y. Ching et al. "The electronic structure and spectroscopic properties of 3C, 2H, 4H, 6H, 15R and 21R polymorphs of SiC". en. In: *Materials Science and Engineering: A*. NANOAM 422.1 (Apr. 2006), pp. 147–156. ISSN: 0921-5093. DOI: 10.1016/j.msea.2006.01.007.

[9] W.E. Spicer et al. "The surface electronic structure of 3–5 compounds and the mechanism of Fermi level pinning by oxygen (passivation) and metals (Schottky barriers)". en. In: *Surface Science* 86 (July 1979), pp. 763–788. ISSN: 00396028. DOI: 10.1016/0039-6028(79)90458-8.

[10] D. J. Ewing et al. “Inhomogeneities in Ni/4H-SiC Schottky barriers: Localized Fermi-level pinning by defect states”. In: *Journal of Applied Physics* 101.11 (June 2007). Publisher: American Institute of Physics. ISSN: 0021-8979. DOI: 10.1063/1.2745436.

[11] Aurangzeb Khan and Yamaguchi Masafumi. “Deep Level Transient Spectroscopy: A Powerful Experimental Technique for Understanding the Physics and Engineering of Photo-Carrier Generation, Escape, Loss and Collection Processes in Photovoltaic Materials”. en. In: *Solar Cells - New Approaches and Reviews*. Ed. by Leonid A. Kosyachenko. InTech, Oct. 2015. ISBN: 978-953-51-2184-8. DOI: 10.5772/59419.

[12] Marianne E. Bathen, Robert Karsthof, and Julie Bonkerud. *DLTS setup Asterix*. 2022.

[13] Silvaco Inc. *Atlas User's Manual*. Aug. 2016.

[14] Philip Ball. “First quantum computer to pack 100 qubits enters crowded race”. en. In: *Nature* 599.7886 (Nov. 2021), pp. 542–542. DOI: 10.1038/d41586-021-03476-5. URL: https://www.nature.com/articles/d41586-021-03476-5 (visited on 03/22/2022).

[15] Øyvind Grøn. *Introduction to Einstein's Theory of Relativity: From Newton's Attractive Gravity to the Repulsive Gravity of Vacuum Energy*. English. 2nd ed. 2020 edition. Cham, Switzerland: Springer, May 2020. ISBN: 978-3-030-43861-6.

[16] Silvaco Inc. *Reverse I-V of SiC Schottky and Junction Barrier Schottky (JBS) Diodes*. en-US. 2021. URL: https://silvaco.com/examples/tcad/index.html (visited on 03/30/2022).

[17] Luigi Di Benedetto et al. “Analytical Model and Design of 4H-SiC Planar and Trenched JBS Diodes”. In: *IEEE Transactions on Electron Devices* 63.6 (June 2016). Conference Name: IEEE Transactions on Electron Devices, pp. 2474–2481. ISSN: 1557-9646. DOI: 10.1109/TED.2016.2549599.

[18] D.M. Caughey and R.E. Thomas. “Carrier mobilities in silicon empirically related to doping and field”. In: *Proceedings of the IEEE* 55.12 (Dec. 1967). Conference Name: Proceedings of the IEEE, pp. 2192–2193. ISSN: 1558-2256. DOI: 10.1109/PROC.1967.6123.

[19] M. Roschke and F. Schwierz. “Electron mobility models for 4H, 6H, and 3C SiC [MESFETs]”. In: *IEEE Transactions on Electron Devices* 48.7 (July 2001). Conference Name: IEEE Transactions on Electron Devices, pp. 1442–1447. ISSN: 1557-9646. DOI: 10.1109/16.930664.

[20] Atsushi Koizumi, Jun Suda, and Tsunenobu Kimoto. "Temperature and doping dependencies of electrical properties in Al-doped 4H-SiC epitaxial layers". In: *Journal of Applied Physics* 106.1 (July 2009). Publisher: American Institute of Physics, p. 013716. ISSN: 0021-8979. DOI: 10.1063/1.3158565.

[21] A. Galeckas et al. "Auger recombination in 4H-SiC: Unusual temperature behavior". In: *Applied Physics Letters* 71.22 (Dec. 1997). Publisher: American Institute of Physics, pp. 3269–3271. ISSN: 0003-6951. DOI: 10.1063/1.120309.

[22] P. Ščajev et al. "Fast and slow carrier recombination transients in highly excited 4H– and 3C–SiC crystals at room temperature". In: *Journal of Applied Physics* 108.2 (July 2010). Publisher: American Institute of Physics, p. 023705. ISSN: 0021-8979. DOI: 10.1063/1.3459894.

[23] U. Lindefelt. "Doping-induced band edge displacements and band gap narrowing in 3C–, 4H–, 6H–SiC, and Si". In: *Journal of Applied Physics* 84.5 (Sept. 1998). Publisher: American Institute of Physics, pp. 2628–2637. ISSN: 0021-8979. DOI: 10.1063/1.368374.

[24] *Work Functions for Photoelectric Effect*. URL: http://hyperphysics.phy-astr.gsu.edu/hbase/Tables/photoelec.html (visited on 04/01/2022).

[25] Ł. Gelczuk et al. "Origin and anomalous behavior of dominant defects in 4H-SiC studied by conventional and Laplace deep level transient spectroscopy". In: *Journal of Applied Physics* 127.6 (Feb. 2020). Publisher: American Institute of Physics, p. 064503. ISSN: 0021-8979. DOI: 10.1063/1.5140731.

[26] Thomas Dalibor et al. "Electrical properties of the titanium acceptor in silicon carbide". In: *Physical Review B* 55.20 (May 1997). Publisher: American Physical Society, pp. 13618–13624. DOI: 10.1103/PhysRevB.55.13618.

[27] Katsuya Takahashi et al. "Carrier Trapping Effects on Forward Characteristics of SiC p-i-n Diodes Fabricated on High-Purity Semi-Insulating Substrates". In: *IEEE Transactions on Electron Devices* 69.4 (Apr. 2022). Conference Name: IEEE Transactions on Electron Devices, pp. 1989–1994. ISSN: 1557-9646. DOI: 10.1109/TED.2022.3154673.

Appendix A

Silvaco Scripts

The following scripts are built and run in Silvaco Deckbuild.

A.1 I-V and C-V Simulations

The script in subsection A.1.3 shows the code used to simulate I-V and C-V characteristics of the diode.

A.1.1 I-V

The code specific to the I-V simulation between 1 and -1 V can be seen on lines 91-95, where the range and step size is specified.

For the breakdown simulations, where the voltage approached -1650 V, the four combinations with and without band-to-band tunneling (line 79) and impact ionisation line 82) was run, where the voltage specification can be seen on lines 98-103.

A.1.2 C-V

The C-V simulations over the 0 to -10 V range is specified on lines 106-110, while the code specific to the simulations of full depletion of the epitaxial layer is on lines 113-117.

A.1.3 Script (I-V and C-V)

```
1  # using diodeex01.in and sicex14.in as templates
2
3  ### Device
4  set epi_thickness=10
5  set buffer_thickness=1.0
```

```
6  set wafer_thickness=30.0
7  set SiC_thickness=$epi_thickness+$buffer_thickness+$wafer_thickness
8  set wafer_width=1000
9  set wafer_width_half=$wafer_width/2
10
11 ### Doping
12 set epi_concentration=1.134e15
13 set buffer_concentration=1e18
14 set wafer_concentration=3e18
15
16 ### File Name
17 set file_string = "Plots_1D_128bit"
18
19 ### Run Atlas
20 go atlas simflags="-128 -p 4"
21
22 ### Mesh
23 mesh space.mult=1
24
25 ##X-mesh
26 x.mesh loc=0.0 spac=$wafer_width/4
27 x.mesh loc=$wafer_width spac=$wafer_width/4
28
29 ##Y-mesh
30 y.mesh loc=0.0 spac=0.01
31 y.mesh loc=0.5 spac=0.04
32 y.mesh loc=$epi_thickness-0.5 spac=0.1
33 y.mesh loc=$epi_thickness spac=0.002
34 y.mesh loc=$epi_thickness+0.02 spac=0.01
35 y.mesh loc=$epi_thickness+$buffer_thickness/2 spac=0.1
36 y.mesh loc=$epi_thickness+$buffer_thickness-0.02 spac=0.01
37 y.mesh loc=$epi_thickness+$buffer_thickness spac=0.002
38 y.mesh loc=$epi_thickness+$buffer_thickness+0.02 spac=0.01
39 y.mesh loc=$epi_thickness+$buffer_thickness+1 spac=0.5
40 y.mesh loc=$SiC_thickness spac=1
41
42 ### Regions
43 ##Makes epitaxal, buffer, and substrate into 4H-SiC
44 region num=1 y.min=0 y.max=$SiC_thickness x.min=0 x.max=$wafer_width
       material=4H-SiC
45
46 ### Electrodes
47 ##Nickel electrode on the top
48 electrode name=anode top
49 ##Back contact
50 electrode name=cathode bottom
```

```
51
52 ### Doping & Material
53 ##Doping of the wafer/substrate
54 doping uniform conc=$wafer_concentration n.type y.min=$epi_thickness +
       $buffer_thickness y.max=$epi_thickness + $buffer_thickness +
       $wafer_thickness
55
56 ##Doping of the buffer layer
57 doping uniform conc=$buffer_concentration n.type y.min=$epi_thickness y.max
       =$epi_thickness + $buffer_thickness
58
59 ##Doping of the epi layer
60 doping uniform conc=$epi_concentration n.type y.min=0 y.max=$epi_thickness
61
62 ##Semiconductor material
63 material material=4H-SiC affinity=3.13 taun0=5.0e-10 taup0=1.0e-10 ARichN
       =146 me.tunnel=0.3 mh.tunnel=0.3 d.tunnel=1.0e-6
64
65 ##Semiconductor mobility
66 mobility material=4H-SiC VSATN=2.2e7 VSATP=1.3e7 MU1N.CAUG=40 MU1P.CAUG=0
       MU2N.CAUG=950 MU2P.CAUG=114 DELTAN.CAUG=0.76 DELTAP.CAUG=0.69 NCRITN.
       CAUG=1e17 NCRITP.CAUG=2.3e18 ALPHAN.CAUG=0 ALPHAP.CAUG=0 BETAN.CAUG=0
       BETAP.CAUG=0 GAMMAN.CAUG=0 GAMMAP.CAUG=0
67
68 ### Contacts
69 ##Schottky contact:
70 # work function found at
71 # http://hyperphysics.phy-astr.gsu.edu/hbase/Tables/photoelec.html
72 contact name=anode workfunction=5.01 surf.rec barrier me.tunnel=0.3 mh.
       tunnel=0.3
73
74 ### Models
75 models analytic fldmob srh auger
76 # bgn.lind
77
78 ##Band-to-Band model included for some breakdown simulations
79 #models analytic fldmob srh auger bgn.lind BBT.STD bb.a=8e7 bb.b=9e6 bb.
       gamma=2.6
80
81 ##Impact statement included for some breakdown simulations
82 #impact aniso e.side be0001=2.18e7  bh0001=2.03e7 ae0001=3.82e8 ah0001=3.10
       e8
83
84 ### Solve & Method
85 method newton climit=1e-4
86
```

```
87  set init_name=$file_string"_Init.str"
88  solve init
89  save outf=$init_name
90
91  ##I-V solve statement
92  set IV_name = $file_string"_IV.log"
93  log outfile=$IV_name
94  solve vanode=1.0 vstep=-0.05 vfinal=-1 name=anode
95  log off
96
97  solve init
98  ##I-V Breakdown solve statements
99  set IV_break_name = $file_string"_IV_break.log"
100 log outfile=$IV_break_name
101 solve vanode=0 vstep=-1 vfinal=-50 name=anode
102 solve vanode=-60 vstep=-10 vfinal=-1650 name=anode
103 log off
104
105 solve init
106 ##C-V solve statement
107 set CV_name = $file_string"_CV.log"
108 log outfile=$CV_name
109 solve vanode=0.25 vstep=-0.25 vfinal=-10 name=anode qscv nocurrent
110 log off
111
112 solve init
113 ##C-V Saturation statement
114 set CV_sat_name = $file_string"_CV_sat.log"
115 log outfile=$CV_sat_name
116 solve vanode=0.0 vstep=-1 vfinal=-500 name=anode qscv nocurrent
117 log off
118
119 quit
```

A.2 Transient Simulations

The script in subsection A.2.5 shows the code used for the single electrode transient simulations, with some small changes for the different CCE tests.

A.2.1 CCE vs Voltage

To calculate the charge collection at different voltages, with the radiation track going through the entire stack and without traps, the script is run with lines 24, 25, and 174 uncommented.

A.2.2 CCE vs Track Length

To calculate the charge collection with different radiation track lengths, with a constant reverse voltage of 500 V and without traps, the script is run with lines 29, 30, and 174 uncommented.

A.2.3 CCE vs Trap Concentration

To calculate the charge collection with different $Z_{1/2}$ trap concentrations with a constant reverse bias of 500 V and the radiation track going through the entire stack, the script can be run with lines 35, 36 and 174 uncommented.

A.2.4 Electron and Hole Concentration

Saving the electron and hole concentration (as well as many other parameters) for all grid points in two dimensions, for every single time step, can be done by including lines 140, 144, 148, 152, 156, 160, and 164 to the solve statement above the respective lines.

A.2.5 Script (Transient)

```
1 # using diodeex01.in and sicex14.in as templates
2
3 ### Device
4 set epi_thickness=10
5 set buffer_thickness=1.0
6 set wafer_thickness=30.0
7 set SiC_thickness=$epi_thickness+$buffer_thickness+$wafer_thickness
8 set wafer_width=1000
9 set wafer_width_half=$wafer_width/2
10
11 ### Doping
12 set epi_concentration=1.134e15
13 set buffer_concentration=1e18
14 set wafer_concentration=3e18
15
16 ### Beam
17 set beam_radius=1
18 set beam_centre=$wafer_width/2
19
20 ### Loops
21
22 ##Voltage Loop
23 set voltage=500
```

```
24 #loop steps=6
25 #assign name=voltage print n.value=(0, 25, 50, 100, 250, 500)
26
27 ##Track Length Loop
28 set beamlength=$SiC_thickness
29 #loop steps=6
30 #assign name=beamlength print n.value=(2, 4, 6, 8, 10, 12)
31
32 ##Trap Loop
33 set defect_conc_val=0
34 set defect_conc_pow=0
35 #set defect_conc_val=1
36 #assign name=defect_conc_pow print n.value=(13, 14, 15, 16, 17, 18, 19, 20)
37 set defect_cm3 = $defect_conc_val*10**$defect_conc_pow
38
39 ###File Name
40 set file_string = "Voltages_"$voltage"V_Z12_"$defect_conc_val"pow"
     $defect_conc_pow"_Beamlength_"$beamlength"um_1D_128bit"
41
42 ###Run Atlas
43 go atlas simflags="-128 -p 4"
44
45 ### Mesh
46 mesh space.mult=1
47
48 ##X-mesh
49 x.mesh loc=0.0 spac=$wafer_width/4
50 x.mesh loc=$beam_centre-$beam_radius*4 spac=$beam_radius
51 x.mesh loc=$beam_centre-$beam_radius spac=$beam_radius/10
52 x.mesh loc=$beam_centre+$beam_radius spac=$beam_radius/10
53 x.mesh loc=$beam_centre+$beam_radius*4 spac=$beam_radius
54 x.mesh loc=$wafer_width spac=$wafer_width/4
55
56 ##Y-mesh
57 y.mesh loc=0.0 spac=0.01
58 y.mesh loc=0.5 spac=0.04
59 y.mesh loc=$epi_thickness-0.5 spac=0.1
60 y.mesh loc=$epi_thickness spac=0.002
61 y.mesh loc=$epi_thickness+0.02 spac=0.01
62 y.mesh loc=$epi_thickness+$buffer_thickness/2 spac=0.1
63 y.mesh loc=$epi_thickness+$buffer_thickness-0.02 spac=0.01
64 y.mesh loc=$epi_thickness+$buffer_thickness spac=0.002
65 y.mesh loc=$epi_thickness+$buffer_thickness+0.02 spac=0.01
66 y.mesh loc=$epi_thickness+$buffer_thickness+1 spac=0.5
67 y.mesh loc=$SiC_thickness spac=1
68
```

```
69  ### Regions
70  ##Makes epitaxal , buffer , and substrate into 4H-SiC
71  region num=1 y.min=0 y.max=$SiC_thickness x.min=0 x.max=$wafer_width
        material=4H-SiC
72
73  ### Electrodes
74  ##Nickel electrode on the top
75  electrode name=anode top
76  ##Back contact
77  electrode name=cathode bottom
78
79  ### Doping & Material
80  ##Doping of the wafer/substrate
81  doping uniform conc=$wafer_concentration n.type y.min=$epi_thickness +
        $buffer_thickness y.max=$epi_thickness + $buffer_thickness +
        $wafer_thickness
82
83  ##Doping of the buffer layer
84  doping uniform conc=$buffer_concentration n.type y.min=$epi_thickness y.max
        =$epi_thickness + $buffer_thickness
85
86  ##Doping of the epi layer
87  doping uniform conc=$epi_concentration n.type y.min=0 y.max=$epi_thickness
88
89  ##Semiconductor material
90  material material=4H-SiC affinity=3.13 taun0=5.0e-10 taup0=1.0e-10 ARichN
        =146 me.tunnel=0.3 mh.tunnel=0.3 d.tunnel=1.0e-6
91
92  ##Semiconductor mobility
93  mobility material=4H-SiC VSATN=2.2e7 VSATP=1.3e7 MU1N.CAUG=40 MU1P.CAUG=0
        MU2N.CAUG=950 MU2P.CAUG=114 DELTAN.CAUG=0.76 DELTAP.CAUG=0.69 NCRITN.
        CAUG=1e17 NCRITP.CAUG=2.3e18 ALPHAN.CAUG=0 ALPHAP.CAUG=0 BETAN.CAUG=0
        BETAP.CAUG=0 GAMMAN.CAUG=0 GAMMAP.CAUG=0
94
95  ### Defects/Traps
96  ##Z_1|2
97  trap region=1 acceptor e.level=0.694 density=$defect_cm3 degen.fac=1 sign
        =2.26e-14 sigp=2.26e-14 y.min=0 y.max=$SiC_thickness
98  ##Ti (not used to calculate final results)
99  #trap region=1 donor e.level=0.170 density=$epi_concentration*0.003 degen.
        fac=1 sign=8.66e-15 sigp=8.66e-15 fast
100
101 ### Contacts
102 ##Schottky contact:
103 # work function found at
104 # http://hyperphysics.phy-astr.gsu.edu/hbase/Tables/photoelec.html
```

```
105 contact name=anode workfunction=5.01 surf.rec barrier me.tunnel=0.3 mh.
        tunnel=0.3
106
107 ### Models
108 models analytic fldmob srh auger bgn.lind
109 ##Band-to-Band model included for some breakdown simulations
110 #BBT.STD bb.a=8e7 bb.b=9e6 bb.gamma=2.6
111
112 ## Include additional outputs to .str type files
113 output RECOMB con.band val.band band.param e.mobility h.mobility
114
115 ### Solve & Method
116 method newton climit=1e-4
117
118 set init_name=$file_string"_Init.str"
119 solve init
120 save outf=$init_name
121
122 ##Set the bias on the different electrodes
123 set IV_name = $file_string"_IV.log"
124 log outfile=$IV_name
125 solve vanode=-1 vstep=-$voltage/5 vfinal=-$voltage name=anode
126 log off
127
128 ### Save 2D files before transient simulations
129 set 2D_name = $file_string"_2D.str"
130 save outf=$2D_name
131
132 ### Radiation Track
133 singleeventupset entry="$beam_centre,0.0,0.0" exit="$beam_centre,
        $beamlength,0.0" pcunits=True density=0 b.density=1.28e-5 radius=
        $beam_radius t0=5.0e-15 tc=1.0e-15
134
135 set transient_name = $file_string"_transient.log"
136 log outf=$transient_name
137
138 method newton DT.MAX=2e-16
139 solve tfinal=1e-14 tstep=1e-16
140 # outfile=$file_string"_t_A.sta" master
141
142 method newton DT.MAX=2e-15
143 solve tfinal=1e-13 tstep=2e-16
144 # outfile=$file_string"_t_B.sta" master
145
146 method newton DT.MAX=1e-13
147 solve tfinal=1e-12 tstep=1e-14
```

```
148 # outfile=$file_string"_t_C.sta" master
149
150 method newton DT.MAX=1e-12
151 solve tfinal=1e-11 tstep=1e-13
152 # outfile=$file_string"_t_D.sta" master
153
154 method newton DT.MAX=1e-11
155 solve tfinal=1e-10 tstep=1e-12
156 # outfile=$file_string"_t_E.sta" master
157
158 method newton DT.MAX=1e-10
159 solve tfinal=1e-9 tstep=1e-11
160 # outfile=$file_string"_t_F.sta" master
161
162 method newton DT.MAX=1e-9
163 solve tfinal=1e-8 tstep=1e-10
164 # outfile=$file_string"_t_G.sta" master
165
166 ## The commented out "outfile" lines are included in the
167 ## line above them to save 2D data for all simulated timesteps
168
169 log off
170
171 ### End loops
172 ##one l.end for each loop to end
173
174 #l.end
175
176 quit
```

A.3 Strip Detector Simulations

The script in subsection A.2.5 shows the code used for transient simulations of the strip electrode design, with three strip electrodes.

A.3.1 Script (Strip)

```
1 # using diodeex01.in and sicex14.in as a templates
2
3 ### Device
4 set epi_thickness=10
5 set buffer_thickness=1.0
6 set wafer_thickness=30.0
7 set SiC_thickness=$epi_thickness+$buffer_thickness+$wafer_thickness
8
```

```
9  set wafer_width=1000
10 set wafer_width_half=$wafer_width/2
11 #set wafer_depth=785.4
12
13 ### Doping
14 set epi_concentration=1.134e15
15 set buffer_concentration=1e18
16 set wafer_concentration=3e18
17
18 ### Loops
19
20 ##Loop over different voltages
21 loop steps=3
22 assign name=voltage print n.value=(100, 200, 400)
23
24 ## Loop over different detector designs
25 loop steps=3
26 assign name=width_strips print n.value=(10, 20, 30)
27 assign name=space_strips print n.value=(10 ,20, 30)
28
29 ### Strips
30 set num_strips=3
31 set grid_strips_edge=0.3
32 set grid_strips_mid=$width_strips/4
33 set grid_space_mid=$space_strips/4
34
35 set start_strips=$wafer_width/2 - ($width_strips*$num_strips +
       $space_strips*($num_strips-1))/2
36
37 ### Beam
38 set beam_radius=1
39 set beam_centre=$start_strips + $width_strips*0.5 + $space_strips*0
40 set num_datapoints=16
41 set pitch=$width_strips + $space_strips
42 set pitch_step=$pitch/$num_datapoints
43 set step_number=0
44 set beam_centre=$beam_centre-$pitch_step
45 set num_steps=$num_datapoints+1
46
47 loop steps=$num_steps
48 set step_number=$step_number+1
49 set beam_centre=$beam_centre+$pitch_step
50 set beam_centre=$start_strips + $width_strips*0.5 + $space_strips*0 +
       $pitch_step*($step_number-1)
51
52 set beamlength=$SiC_thickness
```

```
53
54 ### File Name
55 set file_string = "Microstrips_"$voltage"V_FingerWidth_"$width_strips"
       um_FingerSpace_"$space_strips"um_"StepNumber_$step_number"_128bit"
56
57 ### Run Atlas
58 go atlas simflags="-128 -p 4"
59
60 ### Mesh
61 mesh  space.mult=1
62 x.mesh loc=0 spac=$wafer_width/4
63
64 ##Strips x-mesh
65 set count_strips=0
66 x.mesh loc=$start_strips - $space_strips/2 spac=$grid_space_mid
67 loop steps=3
68 x.mesh loc=$start_strips + $width_strips*$count_strips + $space_strips*
       $count_strips spac=$grid_strips_edge
69 x.mesh loc=$start_strips + $width_strips*($count_strips+0.5) +
       $space_strips*$count_strips spac=$grid_strips_mid
70 x.mesh loc=$start_strips + $width_strips*($count_strips+1) + $space_strips*
       $count_strips spac=$grid_strips_edge
71 x.mesh loc=$start_strips + $width_strips*($count_strips+1) + $space_strips
       *($count_strips+0.5) spac=$grid_space_mid
72 set count_strips=$count_strips+1
73 l.end
74 x.mesh loc=$wafer_width spac=$wafer_width/4
75
76 ##Beam x-mesh
77 x.mesh loc=0.0 spac=$wafer_width/4
78
79 x.mesh loc=$beam_centre-$beam_radius*4 spac=$beam_radius
80 x.mesh loc=$beam_centre-$beam_radius spac=$beam_radius/10
81 x.mesh loc=$beam_centre+$beam_radius spac=$beam_radius/10
82 x.mesh loc=$beam_centre+$beam_radius*4 spac=$beam_radius
83 x.mesh loc=$wafer_width spac=$wafer_width/4
84
85 ##Y-mesh
86 y.mesh loc=0.0 spac=0.01
87 y.mesh loc=0.5 spac=0.04
88 y.mesh loc=$epi_thickness-0.5 spac=0.1
89 y.mesh loc=$epi_thickness spac=0.002
90 y.mesh loc=$epi_thickness+0.02 spac=0.01
91 y.mesh loc=$epi_thickness+$buffer_thickness/2 spac=0.1
92 y.mesh loc=$epi_thickness+$buffer_thickness-0.02 spac=0.01
93 y.mesh loc=$epi_thickness+$buffer_thickness spac=0.002
```

```
94  y.mesh loc=$epi_thickness+$buffer_thickness+0.02 spac=0.01
95  y.mesh loc=$epi_thickness+$buffer_thickness+1 spac=0.5
96  y.mesh loc=$SiC_thickness spac=1
97
98  ### Regions
99  ##Makes epitaxal, buffer, and substrate into 4H-SiC
100 region num=1 y.min=0 y.max=$SiC_thickness x.min=0 x.max=$wafer_width
        material=4H-SiC
101
102 ### Electrodes
103 ##Nickel electrode on the top
104 set count_electrode=0
105 loop steps=3
106 assign name=anode_name print c1="anode1" c2="anode2" c3="anode3"
107 electrode name=$anode_name top x.min=$start_strips + $width_strips*
        $count_electrode + $space_strips*$count_electrode x.max=$start_strips +
        $width_strips*($count_electrode+1) + $space_strips*$count_electrode
108 set count_electrode=$count_electrode+1
109 l.end
110 electrode name=cathode bottom
111
112 ### Doping & Material
113 ##Doping of the wafer/substrate
114 doping uniform conc=$wafer_concentration n.type y.min=$epi_thickness +
        $buffer_thickness y.max=$epi_thickness + $buffer_thickness +
        $wafer_thickness
115
116 ##Doping of the buffer layer
117 doping uniform conc=$buffer_concentration n.type y.min=$epi_thickness y.max
        =$epi_thickness + $buffer_thickness
118
119 ##Doping of the epi layer
120 doping uniform conc=$epi_concentration n.type y.min=0 y.max=$epi_thickness
121
122 ##Semiconductor material
123 material material=4H-SiC affinity=3.13 taun0=5.0e-10 taup0=1.0e-10 ARichN
        =146 me.tunnel=0.3 mh.tunnel=0.3 d.tunnel=1.0e-6
124
125 ##Semiconductor mobility
126 mobility material=4H-SiC VSATN=2.2e7 VSATP=1.3e7 MU1N.CAUG=40 MU1P.CAUG=0
        MU2N.CAUG=950 MU2P.CAUG=114 DELTAN.CAUG=0.76 DELTAP.CAUG=0.69 NCRITN.
        CAUG=1e17 NCRITP.CAUG=2.3e18 ALPHAN.CAUG=0 ALPHAP.CAUG=0 BETAN.CAUG=0
        BETAP.CAUG=0 GAMMAN.CAUG=0 GAMMAP.CAUG=0
127
128 ### Contacts
129 ##Schottky contacts:
```

```
130 # work function found at
131 # http://hyperphysics.phy-astr.gsu.edu/hbase/Tables/photoelec.html
132 loop steps=3
133 assign name=anode_name print c1="anode1" c2="anode2" c3="anode3"
134 contact name=$anode_name workfunction=5.01 surf.rec barrier me.tunnel=0.3
        mh.tunnel=0.3
135 l.end
136
137 ### Models
138 models analytic fldmob srh auger
139 # bgn.lind
140
141 ## Include additional outputs to .str type files
142 output RECOMB con.band val.band band.param e.mobility h.mobility
143
144 ### Solve & Method
145 method newton climit=1e-4
146
147 set init_name=$file_string"_Init.str"
148 solve init
149 save outf=$init_name
150
151 set IV_name = $file_string"_IV.log"
152
153 log outfile = $file_string"_anode1.log"
154 solve vstep=-$voltage/10 vfinal=-$voltage name=anode1
155 log off
156
157 log outfile = $file_string"_anode2.log"
158 solve vstep=-$voltage/10 vfinal=-$voltage name=anode2
159 log off
160
161 log outfile = $file_string"_anode3.log"
162 solve vstep=-$voltage/10 vfinal=-$voltage name=anode3
163 log off
164
165 set 2D_name = $file_string"_2D.str"
166 save outf=$2D_name
167
168 singleeventupset entry="$beam_centre,0.0,0.0" exit="$beam_centre,
        $beamlength,0.0" pcunits=True density=0 b.density=1.28e-5 radius=
        $beam_radius t0=5.0e-15 tc=1.0e-15
169
170 set transient_name = $file_string"_transient.log"
171 log outf=$transient_name
172
```

```
173 method newton DT.MAX=2e-16
174 solve tfinal=1e-14 tstep=1e-16
175 # outfile=$file_string"_t_A.sta" master
176
177 method newton DT.MAX=2e-15
178 solve tfinal=1e-13 tstep=2e-16
179 # outfile=$file_string"_t_B.sta" master
180
181 method newton DT.MAX=1e-13
182 solve tfinal=1e-12 tstep=1e-14
183 # outfile=$file_string"_t_C.sta" master
184
185 method newton DT.MAX=1e-12
186 solve tfinal=1e-11 tstep=1e-13
187 # outfile=$file_string"_t_D.sta" master
188
189 method newton DT.MAX=1e-11
190 solve tfinal=1e-10 tstep=1e-12
191 # outfile=$file_string"_t_E.sta" master
192
193 method newton DT.MAX=1e-10
194 solve tfinal=1e-9 tstep=1e-11
195 # outfile=$file_string"_t_F.sta" master
196
197 method newton DT.MAX=1e-9
198 solve tfinal=1e-8 tstep=1e-10
199 # outfile=$file_string"_t_G.sta" master
200
201 ## The commented out "outfile" lines are included in the
202 ## line above them to save 2D data for all simulated timesteps
203
204 log off
205
206 ### End loops
207 ##one l.end for each loop to end
208
209 l.end
210 l.end
211
212 quit
```